Hyperfine Spectroscopy of Isotopically Engineered Group-IV Color Centers in Diamond

Isaac B.W. Harris,[1,‡] Cathryn P. Michaels,[2,‡] Kevin C. Chen,[1] Ryan A. Parker,[2] Michael Titze,[3] Jesús Arjona Martínez,[2] Madison Sutula,[1] Ian R. Christen,[1] Alexander M. Stramma,[2] William Roth,[2] Carola M. Purser,[2] Martin Hayhurst Appel,[2] Chao Li,[1] Matthew E. Trusheim,[4,1] Nicola L. Palmer,[5] Matthew L. Markham,[5] Edward S. Bielejec,[3] Mete Atatüre,[2,*] and Dirk Englund[1,†]

[1] *Department of Electrical Engineering and Computer Science, Massachusetts Institute of Technology, Cambridge, Massachusetts 02139, USA*

[2] *Cavendish Laboratory, University of Cambridge, Cambridge CB3 0HE, United Kingdom*

[3] *Sandia National Laboratories, Albuquerque, New Mexico 87123, USA*

[4] *DEVCOM, Army Research Laboratory, Adelphi, Maryland 20783, USA*

[5] *Element Six, Global Innovation Centre, Fermi Avenue, Harwell, Didcot OX11 0QR, United Kingdom*

(Received 6 June 2023; accepted 7 August 2023; published 2 October 2023)

A quantum register coupled to a spin-photon interface is a key component in quantum communication and information processing. Group-IV color centers in diamond (SiV^-, GeV^-, and SnV^-) are promising candidates for this application, comprising an electronic spin with optical transitions coupled to a nuclear spin as the quantum register. However, the creation of a quantum register for these color centers with deterministic and strong coupling to the spin-photon interface remains challenging. Here, we make first-principles predictions of the hyperfine parameters of the group-IV color centers, which we verify experimentally with a comprehensive comparison between the spectra of spin active and spin neutral intrinsic dopant nuclei in single GeV^- and SnV^- emitters. In line with the theoretical predictions, detailed spectroscopy on large sample sizes reveals that hyperfine coupling causes a splitting of the optical transition of SnV^- an order of magnitude larger than the optical line width and provides a magnetic field insensitive transition. This strong coupling provides access to a new regime for quantum registers in diamond color centers, opening avenues for novel spin-photon entanglement and quantum sensing schemes for these well-studied emitters.

DOI: 10.1103/PRXQuantum.4.040301

I. INTRODUCTION

Spin-photon interfaces are the backbone for many quantum communication [1–4], transduction [5,6], sensing [7–9], and computing schemes [10,11], with one of the most promising physical implementations being color centers in the solid state [12]. Group-IV color centers in diamond are particularly appealing for spin-photon interfaces, offering excellent optical properties when integrated into nanostructures [13–17], insensitivity to charge noise [18], and high-fidelity spin control [19,20]. In these systems, localized electronic states around a lattice defect provide a local spin qubit, while the transitions between ground and excited electronic orbital energy levels provide optical access for readout, initialization, and spin-photon entanglement generation [20–22].

Central to many color-center-based quantum protocols is the presence of a local quantum register coupled strongly to the spin-photon interface, which allows for the storage of quantum information while spin-photon entanglement operations are being performed [23–25]. The most common implementation of this local register is with a proximal spin-active nucleus of the host lattice, coupled to the electron in the spin-photon interface by hyperfine coupling, such as ^{13}C in diamond [26–28]. ^{13}C memories have been used in demonstrations of quantum networks [3,22,29,30] and even allow for tens of nuclear spin memories coupled to a single spin-photon interface [31]. However, the inclusion of the ^{13}C register is inherently

*ma424@cam.ac.uk
†englund@mit.edu
‡These two authors contributed equally to this work.

nondeterministic, reducing the yield of good quantum registers. Intrinsic dopant nuclear spins, on the other hand, allow for the deterministic inclusion of a quantum register [4,32]. For many applications where a large number of quantum registers is not required, these properties make dopant nuclei easier to integrate into quantum systems that require high-yield high-fidelity control.

While the electronic spin properties of group-IV color centers have been investigated [33–36], the development of a thorough understanding of the coupling to the intrinsic nuclear spin register is needed. Each group-IV element has at least one nuclear isotope with spin $I > 0$ but only the spin-1/2 ^{29}Si in the SiV$^-$ has been used as a memory qubit [4], with a reported ground-state hyperfine coupling of approximately 70 MHz [19,37]. Hyperfine coupling in other group-IV color centers remains understudied, with only a few recent reports of hyperfine coupling, including to the intrinsic nuclear spin of GeV$^-$ [38], to weakly coupled [39] and strongly coupled [20] ^{13}C nuclei using the SnV$^-$ and to the intrinsic nuclear spin of ^{117}SnV$^-$ [40].

In this paper, we develop a detailed model of the intrinsic nuclear memory of group-IV color centers and predict the hyperfine parameters for each group-IV isotope using density-functional theory (DFT). We then compare these predictions with our experimental observations of optical hyperfine signatures for ^{73}GeV$^-$, ^{117}SnV$^-$, and ^{119}SnV$^-$, allowing the assignment of isotopic signatures directly to the optical spectrum. We demonstrate that SiV$^-$, GeV$^-$, and SnV$^-$ have substantially higher hyperfine coupling strengths than NV$^-$ and we capture a proportionality between the hyperfine strength and the atomic mass of the color center. This leads to an optical signature of SnV$^-$ spin-active isotope hyperfine splitting that is 13 times larger than the homogeneous line width of the optical transitions, allowing for direct optical access to the nuclear spin.

II. FIRST-PRINCIPLES MODEL OF GROUP-IV COLOR-CENTER HYPERFINE INTERACTION

Group-IV color centers consist of a single dopant atom from group IV of the periodic table sitting at a D_{3d}-symmetric interstitial site between two neighboring carbon vacancies in the diamond lattice, as shown in Fig. 1(a). The electronic structure is a single hole orbiting the defect [34],

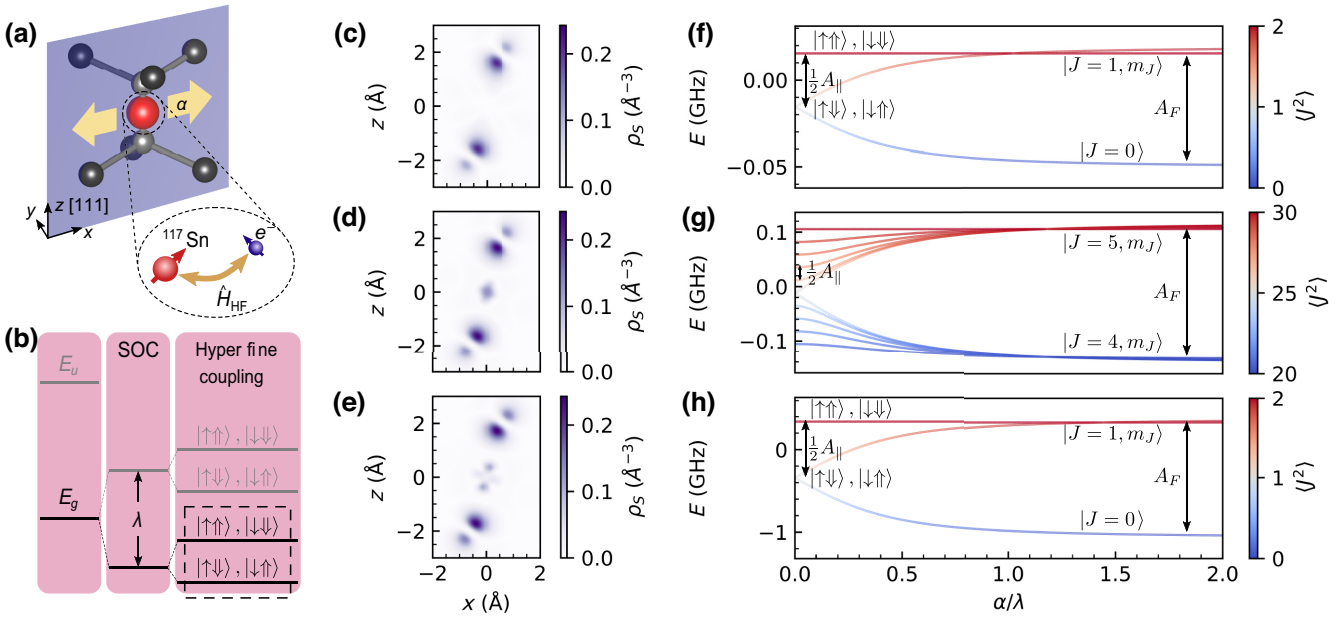

FIG. 1. The first-principles hyperfine structure of group-IV color centers. (a) The split-vacancy structure of a representative group-IV color center, ^{117}SnV$^-$, highlighting the interaction between the electron and nuclear spins. The group-IV dopant is shown in red, the nearest-neighbor carbon atoms in black, and the lattice vacancies in gray. (b) The group-IV color center level structure, showing E_g and E_u manifolds for a spin-1/2 group-IV color center. Spin-orbit coupling (SOC), λ, splits each manifold into two branches (only shown for E_g). The addition of the hyperfine interaction with a spin-1/2 nucleus at zero strain splits each branch into two degenerate levels with aligned or antialigned nuclear and electron spins. (c)–(e) Cross sections of the spin density along the plane shown in (a) for (c) ^{29}SiV$^-$, (d) ^{73}GeV$^-$, and (e) ^{117}SnV$^-$. The presence of a heavier group-IV ion results in an increased spin density at the inversion symmetry center. (f)–(h) The energies of the lower-branch ground-state hyperfine levels as a function of the strain, α, shown in (a) and expressed as a fraction of spin-orbit coupling strength, for (f) ^{29}SiV$^-$, (g) ^{73}GeV$^-$, and (h) ^{117}SnV$^-$. Red and blue indicate the total angular momentum squared of the electronuclear system, $\langle J^2\rangle$, and correspond to the cases when electron and nucleus are aligned or antialigned, respectively.

which exists in a ground E_g or excited E_u state, as illustrated in Fig. 1(b). We model the state of the hole in either manifold as a tensor product of the orbital and spin degrees of freedom, resulting in a basis of the four states

$$\left|\psi_{\mathrm{gnd(exc)}}\right\rangle = \left|e_{g(u)\pm}\right\rangle \otimes |\uparrow / \downarrow\rangle, \tag{1}$$

where the quantization axis of the orbital and spin degrees of freedom is along the D_{3d} symmetry axis. The Hamiltonian for the hole-spin system, $\hat{H}_S$, is a sum of contributions from spin-orbit ($\hat{H}_{\mathrm{SOC}}$), strain ($\hat{H}_{\mathrm{Egx/y}}$), and magnetic field ($\hat{H}_{\mathrm{B/L}}$) coupling. Hence,

$$\hat{H}_S = \hat{H}_{\mathrm{SOC}} + \hat{H}_{\mathrm{Egx}} + \hat{H}_{\mathrm{Egy}} + \hat{H}_B + \hat{H}_L, \tag{2}$$

where, in the basis defined in Eq. (1), $\hat{H}_{\mathrm{SOC}} = \lambda\sigma_z^{\mathrm{orb}}\sigma_z^S/2$, $\hat{H}_{\mathrm{Egx/y}} = -\alpha\sigma_{x/y}^{\mathrm{orb}}$, $\hat{H}_B = g\mu_B\mathbf{B}\cdot\hat{\mathbf{S}}$, $\hat{H}_L = q\mu_B B_z\sigma_z^{\mathrm{orb}}$, g is the electron g factor, μ_B is the Bohr magneton, $\hat{\mathbf{S}} = 1/2(\sigma_x^S, \sigma_y^S, \sigma_z^S)$ is the standard electron spin operator, and $\sigma_i^{\mathrm{orb/S}}$ are the Pauli matrices applied to the orbital or spin degree of freedom. The forms of the four-level Hamiltonian for these perturbations are inferred from group theory [34,41,42], generally up to a constant factor that must be calculated from first principles [36] or measured experimentally [34,43]. We do not model separately the symmetry-breaking Jahn-Teller distortion, as its effects can be absorbed into an effective reduction of the spin-orbit interaction [36].

A. Hyperfine interaction model

The nuclear spin interacts with magnetic field via the nuclear Zeeman interaction

$$\hat{H}_I = g_I\mu_N\mathbf{B}\cdot\hat{\mathbf{I}}, \tag{3}$$

where g_I is the nuclear g factor, μ_N is the nuclear magneton, and $\hat{\mathbf{I}}$ is the standard nuclear spin operator for a spin-I nucleus. To model the hyperfine interaction, we expand the basis in Eq. (1) to include the nuclear spin degree of freedom quantized along the defect axis of symmetry, $|m_I\rangle$. The nucleus interacts with the electronic spin-orbit system via the hyperfine interaction

$$\hat{H}_{\mathrm{HF}} = \hat{\mathbf{S}}\cdot\mathbf{A}\cdot\hat{\mathbf{I}}, \tag{4}$$

where $\mathbf{A} = \mathbf{A}_{\mathrm{FC}} + \mathbf{A}_{\mathrm{DD}}$ is the hyperfine tensor [27,28]. As discussed in Appendix C, the terms $\mathbf{A}_{\mathrm{FC}}$ and $\mathbf{A}_{\mathrm{DD}}$ correspond to the Fermi-contact interaction and the dipole-dipole interaction, respectively.

The Fermi contact is isotropic and so can be expressed as a single scalar parameter A_{FC} multiplied by the identity matrix. For a group-IV nucleus located at the inversion-symmetric point in the color center, the D_{3d} symmetry restricts $\mathbf{A}_{\mathrm{DD}}$ to be a diagonal matrix with elements $A_{\mathrm{DD}} = -2A_{\mathrm{DD}}^{xx} = -2A_{\mathrm{DD}}^{yy} = A_{\mathrm{DD}}^{zz}$ in the frame defined in Fig. 1(a) [44]. Equation (4) then becomes

$$\hat{H}_{\mathrm{HF}} = A_\perp\left(\hat{S}_x\hat{I}_x + \hat{S}_y\hat{I}_y\right) + A_\parallel\hat{S}_z\hat{I}_z. \tag{5}$$

The $A_\parallel = A_{\mathrm{FC}} + A_{\mathrm{DD}}$ term is a shift of the energy levels that depends on the alignment of the electronic and nuclear spins. The $A_\perp = A_{\mathrm{FC}} - 2A_{\mathrm{DD}}$ terms mix states with identical orbital angular momentum but different spin and nuclear quantum numbers. In the absence of other perturbations, the hyperfine levels form two hyperfine manifolds with total angular momentum $J = I \pm S$ separated in energy by $A_\parallel$, with further splitting $3A_{\mathrm{DD}}/2$ between the m_J sublevels within each manifold.

Nuclear spin-orbit and quadrupole coupling, discussed in Appendix D, also result in additional terms in the hyperfine-interaction Hamiltonian. These terms contribute less than 5% of the total hyperfine-interaction strength, so we do not include these in our model. The Jahn-Teller distortion mentioned previously also affects the hyperfine interaction; however, the change in interaction strength is less than 10% of A_{FC} for SiV^-, as discussed in Appendix D. We also exclude this effect from our model on the grounds that it is not strong enough to cause qualitative change in the system. This exclusion also allows us to avoid modeling the vibronic electron-photon modes for computational simplicity.

The final equation for the electronuclear system is the sum of the terms in Eqs. (2), (3), and (5):

$$\hat{H} = \hat{H}_S + \hat{H}_I + \hat{H}_{\mathrm{HF}}. \tag{6}$$

B. Hyperfine parameters from DFT

To estimate the values of $A_{\mathrm{FC/DD}}$, we perform DFT calculations with QUANTUM ESPRESSO [45], as detailed in Appendix C. The resulting spin density in the ground state is plotted in Figs. 1(c)–1(e) for SiV^-, GeV^-, and SnV^- respectively, and the calculated values for the hyperfine parameters are shown in Table I.

Normalizing for the nuclear gyromagnetic ratio, the hyperfine interaction increases with the mass of the group-IV dopant nucleus. This is explained by the increasing contribution of the dopant orbitals compared to the carbon dangling bonds for the heavier elements. The increased dopant orbital contribution to the spin density results in a large spin density near the dopant nucleus and therefore an increased hyperfine interaction. This general trend is also present in other systems, such as group-V donors in silicon [46,47] and molecular systems [48].

C. Effect of strain on hyperfine structure

The electronic spin-orbit interaction, $\hat{H}_{\mathrm{SOC}}$, contained within the $\hat{H}_S$ term, separates states in which the hole spin

TABLE I. A summary of the hyperfine parameters predicted by DFT and measured experimentally.

Isotope	Spin	g_I	A_{FC}^{gnd} (DFT, MHz)	A_{DD}^{gnd} (DFT, MHz)	A_{FC}^{exc} (DFT, MHz)	A_{DD}^{exc} (DFT, MHz)	A_{PLE} (DFT, MHz)	A_{PLE} (experimental, MHz)	DFT error (%)
^{29}Si	1/2	−1.110	64.20	−2.34	−30.68	32.57	−29.98	···	···
^{73}Ge	9/2	−0.195	48.23	−1.35	5.03	14.30	−13.78	−12.5(5)	9.2
^{115}Sn	1/2	−1.836	1275.04	−24.47	386.74	230.43	−316.70	···	···
^{117}Sn	1/2	−2.000	1389.09	−26.65	421.34	251.05	−345.02	−445(9)	22
^{119}Sn	1/2	−2.092	1453.27	−27.89	440.80	262.65	−360.96	−484(8)	26

is aligned or antialigned with the orbital angular momentum by an amount λ, as shown in Fig. 1(b). The hyperfine shift due to the $A_\parallel$ term remains unaffected by this spin-orbit splitting. However, the splitting also means that the upper and lower branches contain states with opposite $e_{g(u)\pm}$ orbital character. As the $A_\perp$ terms can only mix states with the same orbital character, in the limit of $\lambda \gg A_\perp$, these terms are perturbatively suppressed. The eigenstates cease to have well-defined total angular momentum and are simply of the form $|e_{g(u)\pm}\rangle\,|\uparrow/\downarrow\rangle\,|m_I\rangle$, with eigenvalues separated by $A_\parallel/2$, as can be seen in Fig. 1(b).

When transverse $E_{gx(y)}$ strain is introduced into the system, as parametrized by the amount of strain α (β), the upper and lower orbital states are further mixed together. The hyperfine levels are affected by the orbital mixing, as shown in Figs. 1(f)–1(h) for E_{gx} strain using the DFT ground-state values for ^{29}SiV$^-$, ^{73}GeV$^-$, and ^{117}SnV$^-$. E_{gy} strain only changes the orbital character of the orbitals in the upper or lower branch and has an identical effect on the hyperfine energy levels. In the limit of large strain $\alpha, \beta \gg \lambda$, the upper and lower branches have well-defined orbital character and the $A_\perp$ hyperfine terms are again able to mix the states $|\uparrow/\downarrow\rangle\,|m_I\rangle$ within each branch. Each orbital branch then separates into two hyperfine manifolds of well-defined total spin angular momentum J, separated by A_{FC} and with a spacing of $3A_{DD}/2$ between the m_J sublevels. The isotopes ^{29}Si and ^{117}Sn are spin-1/2 nuclei and as such they exhibit splitting into $J = 0$ singlet and $J = 1$ triplet states, whereas the spin-9/2 ^{73}Ge nucleus has a more complicated splitting into $J = 4$ and $J = 5$ states.

D. Hyperfine structure in optical spectra

The strength of the optical transitions is proportional to the matrix element $\langle\psi_{exc}|\hat{d}|\psi_{gnd}\rangle$, where $\hat{d}$ is the electric dipole operator. Since $\hat{d}$ only acts on the orbital degree of freedom [34], optical transitions cannot flip the nuclear or electronic spins and only the spin-conserving transitions contribute significantly to the transition (see Appendix E).

We are in the limit of large spin-orbit coupling, where the electronuclear ground-state Hamiltonian in Eq. (6) produces a series of equally spaced hyperfine levels in both the upper and lower branches of the ground state, separated by $A_\parallel^{gnd}/2 = (A_{FC}^{gnd} + A_{DD}^{gnd})/2$. Similarly, the excited state has hyperfine levels equally spaced by $A_\parallel^{exc}/2$. The net effect on photoluminescence excitation (PLE) experiments is to split the C transition into a series of hyperfine transitions, with an optical spacing $A_{PLE} = (A_\parallel^{exc} - A_\parallel^{gnd})/2$.

For the spin-1/2 isotopes discussed in this paper, the hyperfine interaction results in four total transitions. At zero strain, these occur in two degenerate pairs separated by A_{PLE}: at lower frequency between the $m_J = \pm 1$ hyperfine states in the ground or excited level (C_{H1}) and between the two $m_J = 0$ states at a higher frequency (C_{H0}). The two peaks and their splitting A_{PLE} are labeled for ^{117}SnV$^-$ in Fig. 2(a). The $m_J = \pm 1$ states are unaffected by strain, while the $m_J = 0$ states mix and separate in both ground and excited manifolds. The strain-induced mixing splits the C_{H0} peak in the spectrum into two peaks, labeled C'_{H0} and C''_{H0}, each having half the intensity of the C_{H1} peak, with a splitting δ labeled in Fig. 2(a). The predicted hyperfine interaction for SnV$^-$ is 10 times larger than the expected 35 MHz lifetime-limited line width of the transition [39], making the hyperfine transitions directly resolvable.

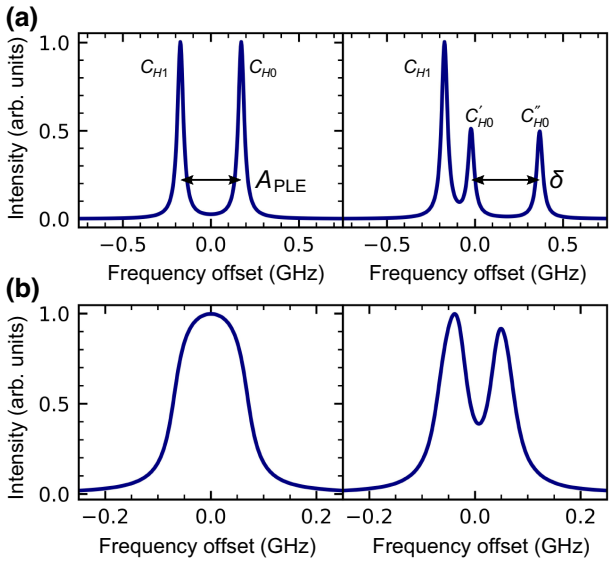

FIG. 2. Predicted spectra using DFT parameter and lifetime-limited line widths for (a) ^{117}SnV$^-$ and (b) ^{73}GeV$^-$ at zero strain in the left panel and a strain $\alpha/\lambda = 0.15$ in the right panel.

Similarly, for the spin-9/2 ^{73}Ge isotope, we expect 20 hyperfine transitions, in ten degenerate pairs that are equally spaced by A_{PLE}. The hyperfine parameters predicted by DFT for ^{73}GeV$^-$ are small because of the small gyromagnetic ratio of ^{73}Ge compared to the other group-IV elements, with the Fermi-contact parameter predicted to be 48 MHz in the ground state. The resulting $A_{\mathrm{PLE}} = -13.78$ MHz is smaller than the expected lifetime-limited line width for GeV$^-$ of 26 MHz [49] and the hyperfine level is therefore not predicted to be optically resolvable. Nevertheless, the overlapping transitions result in a spectral line broadened by approximately $9|A_{\mathrm{PLE}}| = 124$ MHz with a very non-Lorentzian flat-topped line shape. Strain splits the flat-topped emission peak into two peaks corresponding to the transitions between the $J = 5$ levels at lower energy and the $J = 4$ levels at higher energy [see Fig. 2(b)].

The complete hyperfine model of the group-IV color centers discussed in this section gives a unique isotopic spectral signature for each emitter, which we expect to be able to measure experimentally. Some further discussion on the effects of strain on the hyperfine spectrum is found in Appendix E.

III. ISOTOPE-SELECTIVE SPECTROSCOPY

To identify the spectroscopic signature of the group-IV color centers, we prepared diamond plates with isotope-selective implantation of Si, Ge, and Sn, with isotope regions identified by the QR codes etched into the sample [50] (for more details, see Appendix A). A high-temperature annealing process combines the group-IV dopant with a vacancy to form the group-IV color center.

Figure 3(a) shows the four possible transitions between the spin-orbit split levels of group-IV color centers, labeled A through D, which are optically addressable, with the exact frequency of these transitions depending on which group-IV dopant is present in the color center and the residual strain in the sample. In addition, the exact isotope of the dopant also affects the transition energy, with a $\sqrt{M}$ dependence on the isotope mass due to differences in the vibrational ground-state energy [51]. To demonstrate this, we took photoluminescence (PL) measurements and fitted a Gaussian line shape to the C zero-phonon line (ZPL) peak of several ensembles of emitters in order to extract the central frequency.

Figure 3(b) shows the distribution of this extracted central PL frequency for both ^{28}SiV$^-$ and ^{29}SiV$^-$. A clear shift of 83(8) GHz in the central frequency can be seen, which is in good agreement with previous observation of 87 GHz [51]. This shift allows for the differentiation between the two isotopes without isotope selective implant and therefore the selection of a ^{29}SiV center to make use of the spin-1/2 nucleus [4].

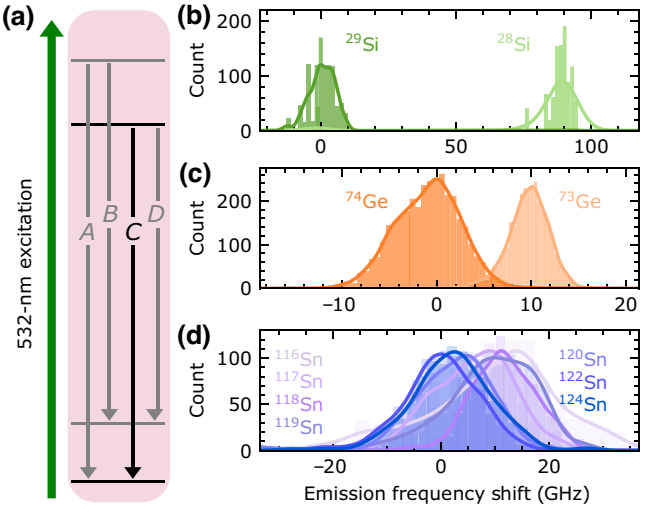

FIG. 3. The characterization of the isotope-dependent photoluminescence. (a) The level structure of the group-IV color centers and photoluminescence transitions. (b)–(d) The distribution of the frequency shift of the C transition for ensembles of (b) SiV$^-$, (c) GeV$^-$, and (d) SnV$^-$. The solid lines are the Gaussian-kernel density estimates.

Figure 3(c) shows the same measurement for ^{73}GeV$^-$ and ^{74}GeV$^-$. A shift of 13(7) GHz can be seen, in line with previous experimental results of 15 GHz [52,53] and predictions based on the expected $\sqrt{M}$ dependency [51]. This means that distinguishing single GeV$^-$ centers using nonresonant excitation is unlikely, given that the GeV$^-$ centers typically have an inhomogeneous distribution of emission of several tens of gigahertz [54].

Similar measurements across seven isotopes of SnV$^-$ are shown in Fig. 3(d). The shift of the ZPL is hidden within the inhomogeneous distributions of each isotope. The model and previous experimental results would suggest a shift between neighboring isotopes of approximately 10 GHz [55]. This is below the resolution of the spectrometer used to measure the PL in this experiment, which combined with inhomogeneous distribution and nonresonant power broadening [56], masks the isotope shift. The shift between isotopes further apart in mass is also hidden, likely due to the imperfect mass selectivity, which brings these ensemble PL distributions toward a central value.

IV. HYPERFINE PHOTOLUMINESCENCE EXCITATION SPECTRA

To quantify the hyperfine parameters experimentally, we performed PLE on the isotope-selectively implanted samples (see Appendix B). We collected statistics on color centers by performing wide-field PLE (WFPLE) experiments [50] on regions of the sample with ^{73}GeV$^-$, ^{74}GeV$^-$, ^{117}SnV$^-$, ^{118}SnV$^-$, ^{119}SnV$^-$, and ^{120}SnV$^-$ with an implant dose of approximately 100 ions per site [57].

This dose is sufficiently low that each site should only contain between one and five emitters given color-center creation yields of approximately 1–5% [15]. This may be further improved with recently developed *in situ* photoluminescence spectroscopy for the formation of deterministic yield emitter arrays [58]. Given the large inhomogeneous line width compared to the typical homogeneous line width, we expect fewer than 0.1% of emitters to have spectrally overlapping emission peaks within the same site.

A. PLE spectroscopy of GeV

For the $I = 9/2$ nucleus of $^{73}GeV^-$, we expect ten overlapping spin-conserving transitions at zero field, as shown in Fig. 4(a) and discussed in Sec. II. When comparing the average WFPLE spectra of 242 $^{73}GeV^-$ emitters and 195 $^{74}GeV^-$ emitters in Fig. 4(b), we see that the $^{73}GeV^-$ spectrum is substantially broader. In Fig. 4(c), we plot a histogram of the Lorentzian line-width fits of the $^{73/74}GeV^-$ emitters and see that the average line width for $^{73}GeV^-$ is 262(7) MHz, roughly 70 MHz broader than the 190(5)-MHz average line width for $^{74}GeV^-$ under the same laser power.

To confirm that this broadening is a result of overlapping hyperfine transitions, we performed confocal PLE using chirped optical resonance excitation (CORE) [17] (see Appendix B) on a $^{73}GeV^-$ emitter at varying magnetic field, shown in Fig. 4(d). We fitted these data using the optical model of the isotope developed in Sec. II, varying only the line width and A_{PLE}. These are found to be 72(3) MHz and 12.5(5) MHz, respectively, within 10% of the DFT prediction. At zero field, the PLE spectrum with near-lifetime-limited line width exhibits a flat-topped line shape due to the overlapping transitions (see Appendix E). As the magnetic field is increased, the electronuclear levels separate into spin-aligned and spin-antialigned groups of energy levels. At around 0.1 T, only the transitions from the two groups near zero detuning still overlap and a characteristic central hump surrounded by two broad shoulders appears, further highlighting that this line shape comes from multiple overlapping hyperfine transitions.

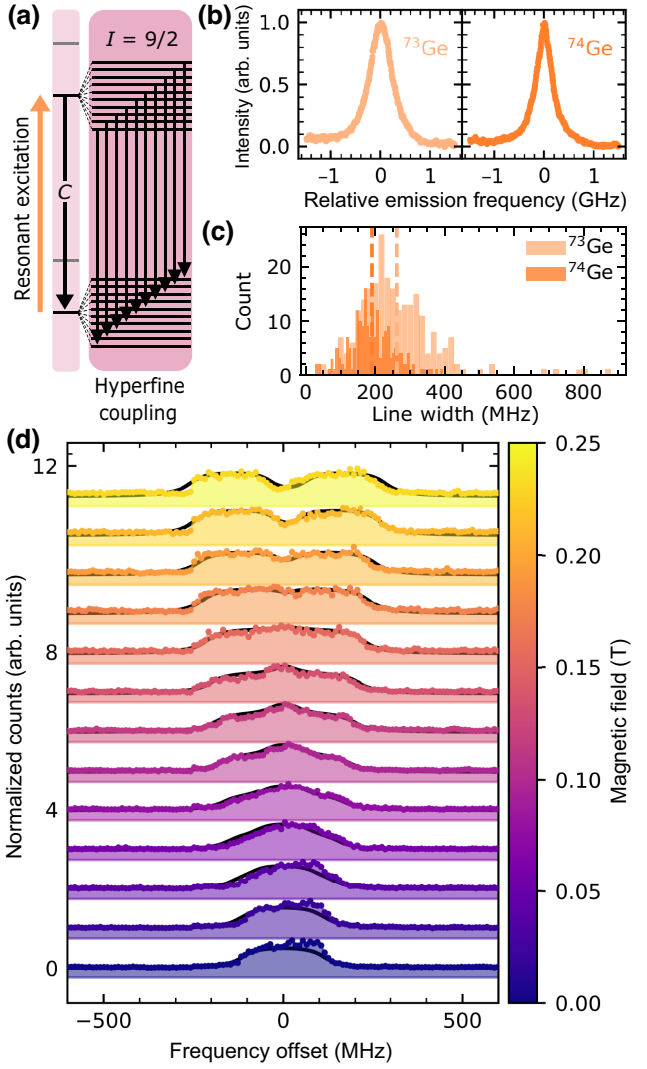

FIG. 4. The hyperfine characterization of GeV^- through PLE. (a) The hyperfine level structure of the spin-9/2 $^{73}GeV^-$ electronuclear system. (b) The average WFPLE spectrum for $^{73}GeV^-$ and $^{74}GeV^-$. (c) The distribution of the emitter line widths for $^{73/74}GeV^-$, showing the larger line width of $^{73}GeV^-$. (d) The PLE spectrum of a $^{73}GeV^-$ emitter in the low-power regime, as a function of the magnetic field at 33° to the high symmetry axis, showing a top-hat line shape. The fit is shown in black.

B. PLE spectroscopy of SnV

As discussed in Sec. II, for SnV^- spin-1/2 isotopes we expect multiple spectrally distinct hyperfine transitions directly observable in the PLE spectra, as illustrated in Fig. 5(a). This is shown experimentally in the average WFPLE spectra averaged over approximately 100 emitters for each of the isotopes $^{117}SnV^-$, $^{118}SnV^-$, $^{119}SnV^-$, and $^{120}SnV^-$ in Fig. 5(b). It is clear that additional spectral features appear for the two spin-1/2 isotopes ^{117}Sn and ^{119}Sn that are not present for the spin-0 isotopes ^{118}Sn and ^{120}Sn.

We fit the PLE spectrum for each SnV^- individually with either a single Lorentzian peak (representing a spin-0 isotope) or three Lorentzian peaks with a 2:1:1 intensity ratio (corresponding to a spin-1/2 isotope). For each spin-1/2 isotope fit, we extract the parameters A_{PLE} and δ, as illustrated for a representative emitter in Fig. 5(c). The three-peak hyperfine feature is observed for more than 80% of the emitters in the two spin-1/2 isotope-implanted regions, whereas it is present in less than 20% of the emitters in the spin-0 isotope-implanted regions (see Table II). Performing a χ^2 test on the number of emitters with the multipeak PLE spectra in the spin-0 versus spin-1/2

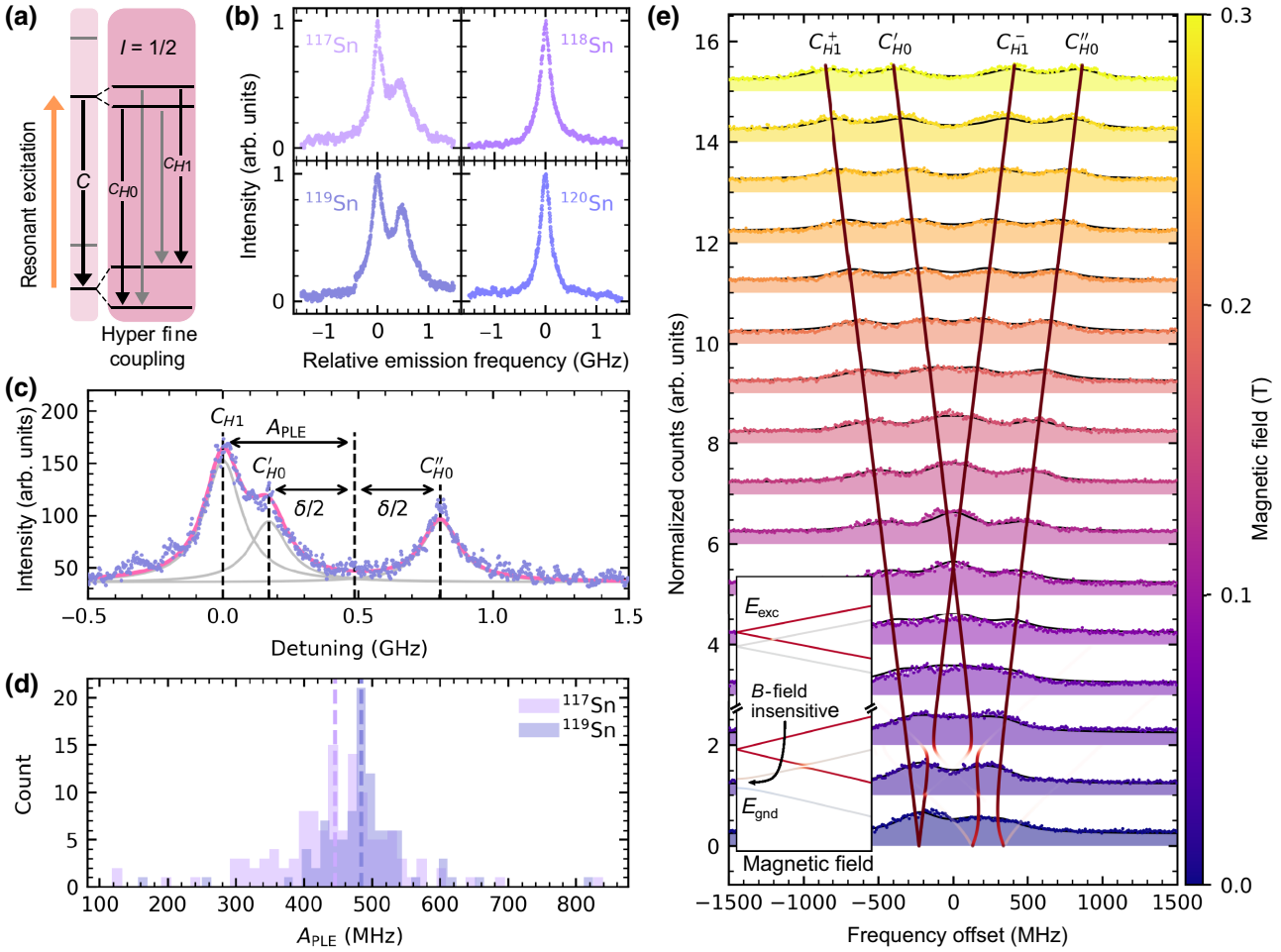

FIG. 5. The hyperfine characterization of SnV^- via PLE. (a) The hyperfine level structure of a spin-1/2 SnV^- electronuclear system. (b) The averaged WFPLE spectrum for $^{117}SnV^-$, $^{118}SnV^-$, $^{119}SnV^-$, and $^{120}SnV^-$. (c) A typical WFPLE spectrum (purple) of a strained $^{119}SnV^-$, showing the hyperfine peaks with relative heights 2:1:1 (gray), split by the hyperfine parameter A_{PLE} and strain parameter δ, with the combined fit with all transitions in pink. The peaks are labeled C'_{H0}, C''_{H0}, and C_{H1} as explained in the text. (d) The histogram of the optical hyperfine splitting A_{PLE} for the spin-1/2 nuclei $^{117/119}SnV^-$. (e) The PLE spectrum of a $^{117}SnV^-$ emitter as a function of the magnetic field, with the fit in black, showing the three peaks at zero field split into four peaks labeled C^+_{H1}, C^-_{H1}, C'_{H0}, and C''_{H0}. Transition frequencies from the fit are overlaid in red, highlighting the avoided crossing of the C_{H0} transitions near zero field. The inset shows an illustration of the ground- and excited-level structure, with avoided crossings at zero magnetic field.

regions, we conclude with a high degree of certainty that the multipeak PLE is associated with the spin-1/2 isotopes ($p < 10^{-5}$). The bulk of the emitters of the wrong type likely come from imperfect isotope separation during the implantation (see Appendix A). We therefore assign the multipeak feature to the spin-1/2 isotopes of tin. This result is also in line with measurements performed on $^{117}SnV^-$ in nanophotonic structures [40], and clarifies a previous report of SnV^- hyperfine-interaction strength of 40 MHz [20]. We now assess this later report as being due to the hyperfine coupling to a nearest-neighbor ^{13}C nucleus, since it is closer in magnitude to previous predictions for ^{13}C hyperfine coupling [28].

The distribution of the hyperfine parameter A_{PLE} for $^{117}SnV^-$ and $^{119}SnV^-$ are shown in Fig. 5(d) and the mean value is summarized for all isotopes in Table II. We note that A_{PLE} is larger for ^{119}Sn than it is for ^{117}Sn. This is to be expected, since the hyperfine coupling parameters are directly proportional to the nuclear gyromagnetic ratios

TABLE II. The hyperfine statistics for the different SnV^- isotopes. Bold entries highlight spin-active isotopes.

Isotope	Spin	Number of emitters	Fraction with hyperfine peaks (%)	A_{PLE} (SE) (MHz)
^{117}Sn	**1/2**	**136**	**87.5**	**445(9)**
^{118}Sn	0	119	16.0	···
^{119}Sn	**1/2**	**109**	**84.4**	**484(8)**
^{120}Sn	0	93	6.4	···

[27]. We find the ratio $A_{\mathrm{PLE},^{119}\mathrm{Sn}}/A_{\mathrm{PLE},^{117}\mathrm{Sn}} = 1.09(0.04)$ to be in agreement with $g_{^{119}\mathrm{Sn}}/g_{^{117}\mathrm{Sn}} = 1.05$.

We next performed PLE measurements at varying magnetic field on a strained $^{117}\mathrm{SnV}^-$ within a different device, detailed in Appendix B 3, with the results shown in Fig. 5(e). We fit these data using the hyperfine model from Sec. II, finding $A_{\mathrm{PLE}} = -459(3)$ MHz, $\alpha = 55(3)$ GHz, and a power-broadened line width of 336(3) MHz. The simpler level structure compared to $^{73}\mathrm{GeV}^-$ allows us to directly track the trajectory of the transitions as a function of the field strength. The magnetic field breaks the degeneracy of the two constituent transitions of the C_{H1} peak, producing two peaks labeled $C_{H1}^{\pm}$, corresponding to transitions between the ground and excited $m_J = \pm 1$ total-angular-momentum states. Due to the combined effect of an anticrossing of the $m_J = 0$ ground states at zero magnetic field and the much weaker anticrossing of the $m_J = 0$ excited states [see Fig. 5(e), inset], the C_{H0} transitions exhibit an anticrossing near zero field. For a sufficiently strained emitter, such as the $^{119}\mathrm{SnV}^-$ in Fig. 5(c), the strong coupling maintains optical access to the hyperfine levels at this ground-level anticrossing point. Operating at this anticrossing makes the levels magnetically insensitive to first order, suppressing the effect of magnetic noise [59–61]. Nuclear spin-bath magnetic noise has been shown to have a large effect on the coherence of group-IV color centers in previous work [20,22,62], so operating in such a regime may improve coherence.

V. DISCUSSION AND CONCLUSIONS

Our microscopic model of the electronuclear system and the first-principles calculations present a full theoretical framework for understanding the hyperfine coupling of the negatively charged group-IV color centers in diamond. We predict a large increase in the hyperfine parameters moving down the group-IV column of the periodic table due to the increasing contribution of the dopant orbitals to the spin density. We further show that spin-orbit coupling and strain must both be accounted for when modeling the resulting hyperfine levels.

Using isotope-selective ion implantation of group-IV elements in diamond, we are able to identify the optical hyperfine signatures of $^{73}\mathrm{GeV}^-$, $^{117}\mathrm{SnV}^-$, and $^{119}\mathrm{SnV}^-$. In particular, the spin-active SnV^- color centers show a clearly resolvable optical multipeak feature compared to the spin-neutral isotopes due to the large hyperfine coupling to the intrinsic tin nucleus. The hyperfine parameters and resulting PLE features predicted from DFT, as well as the measured PLE features are shown in Table I. The first-principles predictions are in sufficiently good agreement (within approximately 20%) to prove instructive in identifying the hyperfine signatures. The remaining discrepancy between theory and experiment is likely due to the simplifications made in the modeling, such as the exclusion of Jahn-Teller distortion, and the use a local functional instead of a more sophisticated hybrid functional.

Both the GeV^- and SnV^- nuclear registers bring interesting challenges and opportunities for quantum information applications. The spin-9/2 memory in $^{73}\mathrm{GeV}^-$ has a ten-level nuclear memory, allowing for the possibility of the generation of large cluster states by making use of the local memory [23]. Its nuclear quadrupole moment also means that the nuclear spin can potentially be driven directly by an electric field [63].

While the SnV^- isotopes have a more conventional spin-1/2 intrinsic memory, the strong hyperfine coupling means that the hyperfine levels can be accessed optically at zero field. With nonzero strain applied to the defect at this zero-field operating point, our model predicts a magnetic field insensitive transition between the $|J = 0/1, m_J = 0\rangle$ ground states. These states could thus combine the key attributes of a spin-photon interfaces: strong, direct, and stable optical transitions; environmentally insensitive hyperfine "clock states"; and additional hyperfine states for quantum memory. The direct optical access to the hyperfine levels also allows for the possibility of direct transfer of photon states to the nuclear memory without using the electron spin as an intermediary, which may enhance spin-photon entanglement fidelity compared to existing schemes [4]. Optical initialization and readout of the nuclear spin via this hyperfine optical transition has been demonstrated in a separate work [40].

The presence of the strongly coupled memory in the well-established group-IV color-center platform will allow future experiments to leverage their bright high-quality optical emission in a new regime of quantum experiments. The clear identification of the hyperfine parameters of GeV^- and SnV^- in this paper therefore sets the implementation roadmap for future work to use these nuclear spins as local memories for quantum information applications.

More generally, the theory and experimental methods developed here also present a new route to tailor other spin-photon interfaces where the interplay between spin-orbit coupling, crystal strain, and hyperfine interaction may also be important. These include color centers in other material systems, such as silicon [64,65], silicon carbide [66–68], rare-earth elements implanted in solids [60], and other emerging material platforms [69]. This paper demonstrates that the selection of dopant isotopes can have a large effect on the resulting color-center properties through the hyperfine structure. Given the wide availability of isotopically selective implantation, we see this as a useful tool and future standardized step in the fabrication of spin-photon interfaces.

ACKNOWLEDGMENTS

This work was supported in part by the National Science Foundation (NSF) Science-Technology Center (STC) Center for Integrated Quantum Materials (CIQM) under Grant No. DMR-1231319, by the NSF Engineering Research Center for Quantum Networks (CQN) awarded under Cooperative Agreement No. 1941583, and by the MITRE Moonshot Program. We also acknowledge support from the European Research Council (ERC) Advanced Grant "Photon-photon and spin-spin Entanglement using Diamond-based impurity Elements: Silicon, Tin And Lead" (PEDESTAL) (884745), the European Union Quantum Flagship 2D-SIPC. C.P.M. acknowledges support from the Engineering and Physical Sciences Research Council (EPSRC) Doctoral Training Partnerships (DTP), R.A.P. from the General Sir John Monash Foundation and a G-research Grant, J.A.M. from the Winton Programme and the EPSRC DTP, and A.M.S. from EPSRC–Networked Quantum Information Technologies (NQIT). This work was performed, in part, at the Center for Integrated Nanotechnologies, an Office of Science User Facility operated for the U.S. Department of Energy (DOE) Office of Science. Sandia National Laboratories is a multimission laboratory managed and operated by National Technology & Engineering Solutions of Sandia, LLC, a wholly owned subsidiary of Honeywell International, Inc., for the U.S. DOE's National Nuclear Security Administration under Contract No. DE-NA-0003525. The views expressed herein do not necessarily represent the views of the U.S. DOE or the United States Government. M.S. acknowledges support from the NASA Space Technology Graduate Research Fellowship Program. We would additionally like to thank Hamza Raniwala and Hyeongrak Choi for helpful discussions.

I.B.W.H and C.P.M. contributed equally to this work.

APPENDIX A: SAMPLE PREPARATION

We prepared two samples, UC1 and UC2, from single-crystal diamond plates ([N]< 5 ppb) purchased from Element Six. We removed the top 7 μm of diamond with Ar-Cl_2 and O_2 reactive-ion etch (RIE) to relieve the strained surface layer. Subsequently, we deposited 180 nm of silicon nitride as a hard mask and patterned alignment markers and QR codes [50] using electron-beam lithography. A thin layer of gold (approximately 50 nm in thickness) was

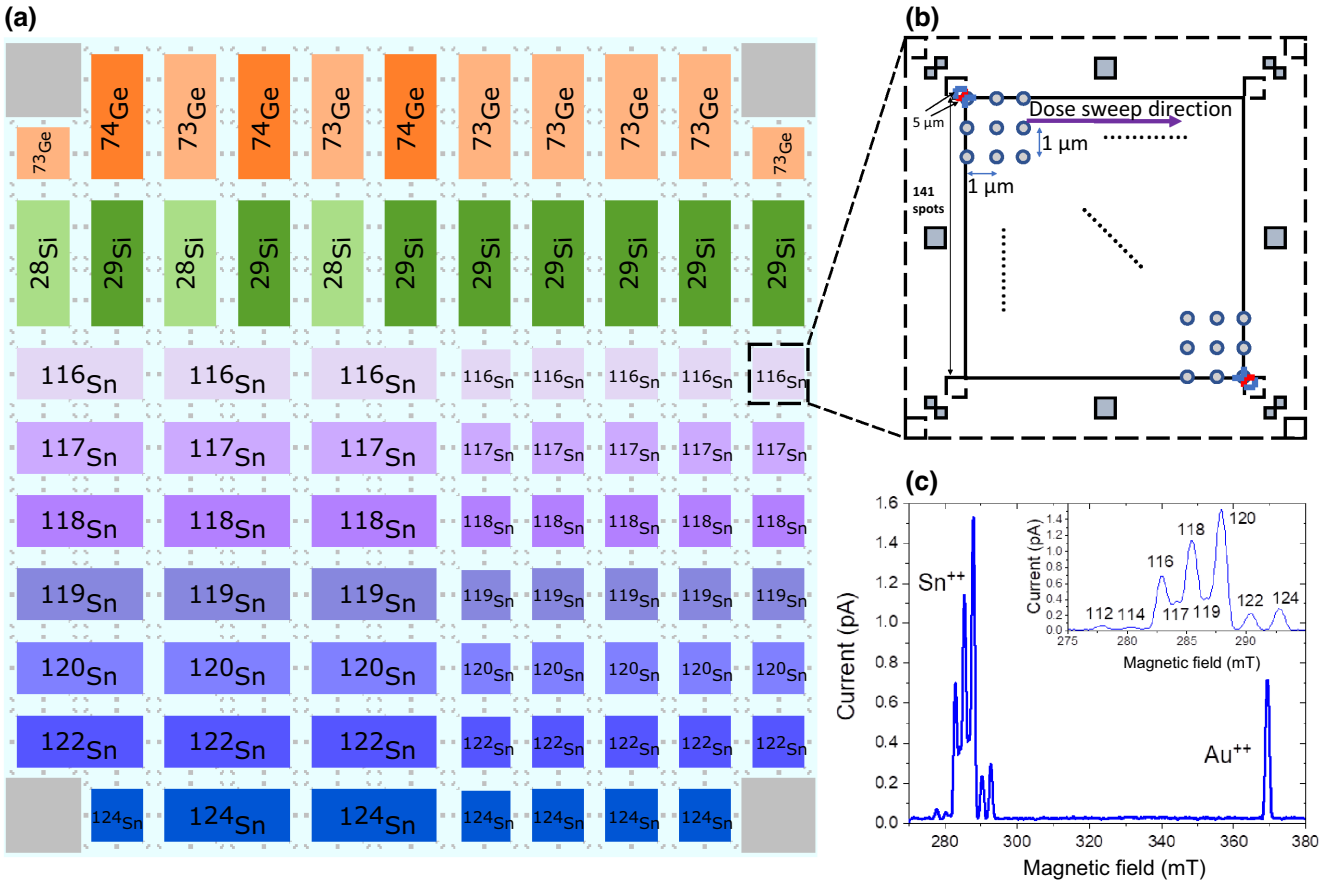

FIG. 6. (a) A diagram of the isotope implantation of the UC1 sample. The QR codes are shown as small gray squares within the implant regions. (b) A diagram of the grid implant pattern. (c) The mass spectrogram of the Sn isotopes.

then deposited and lifted off in HF acid, leaving metal covering only the alignment markers for optimal imaging contrast crucial for alignment during the subsequent ion-implantation step.

The samples were implanted with group-IV elements using a focused-ion-beam (FIB) tool at the Ion Beam Laboratory at Sandia National Laboratory. Specifically, we selectively implanted different isotopes of Si, Ge, and Sn: ^{28}Si, ^{29}Si, ^{73}Ge, ^{74}Ge, ^{116}Sn, ^{117}Sn, ^{118}Sn, ^{119}Sn, ^{120}Sn, ^{122}Sn, and ^{124}Sn in different regions aligned to the QR codes in the sample, as shown in Fig. 6(a) for UC1. UC2 was implanted in a similar manner, with the arrangement of the implant zones varied to fit the slightly larger diamond plate. Each element was implanted at two different energies corresponding to target implant depths of 25 nm and 75 nm. The isotopic separation was not perfect, particularly for the Sn isotopes, which have a small relative isotopic mass difference, as shown in Fig. 6(c). We used the position selectivity of FIB to implant the dopants in a regular grid with 1-μm pitch, and a logarithmically increasing implant dose moving to the right in the sample, as shown in Fig. 6(b). The implant dose range was also swept from region to region, with doses swept between 10 and 10^5, 10^6, 10^7, and 10^8 ions per spot in different regions. Hence, we had a mix of spin neutral and spinful isotopes for each group-IV element in clearly marked spatially separated regions.

Following the implantation, the dopants were converted to group-IV color centers via a high-temperature anneal at 1200°C in ultrahigh vacuum ($<10^{-8}$ mBar) for sample UC1 and a high-pressure high-temperature treatment (>7 GPa at 1950°C) by Element Six. This HPHT anneal was used to improve the emitter characteristics, narrowing the inhomogeneous distribution and improving charge stability [55,70].

APPENDIX B: EXPERIMENTAL SETUP

The nonresonant photoluminescence (PL) measurements presented in Figs. 3(b)–3(d) and the resonant magnetic field dependent measurements presented in Fig. 4(d) were taken on sample UC1, using setup one. The WFPLE experiments presented in Figs. 4(b), 4(c) and Figs. 5(b)–5(d) were taken on sample UC2 in setup two. The magnetic field dependent PLE measurements presented in Fig. 5(e) were taken on sample UC3, using setup three.

1. Setup one

Setup one is outlined in Fig. 7. The diamond sample was housed in a closed-cycle cryostat (attoDRY 2100XL) with a base temperature of 1.7 K. Superconducting coils around the sample space facilitated the application of a two-axis vector magnetic field, with a maximum applied field of 9 T in the z direction, parallel to the length of the cryostat, and a maximum vector field of 3 T in the x direction, parallel to the base of the cryostat. The sample was situated on a three-axis piezoelectric stack (ANPx101/LT and ANPz101/LT), used to move the area of interest beneath a 0.82-numerical-aperture objective. A $4f$ lens system was installed within the cryostat and a confocal microscope sat atop the cryostat, with a motorized mirror used to scan the excitation and collection paths of approximately 50 μm^2 across the diamond sample to collect nonresonant hyperspectral maps. Nonresonant light was provided by a 532-nm laser pen (Roithner Lasertechnik CW532-100), while resonant light at 602 nm was provided by a Toptica DL SHG Pro, tunable between 600 and 620 nm. Resonant excitation was filtered from the collection path using a long-pass filter (Semrock BLP01-633R-25), tuned such

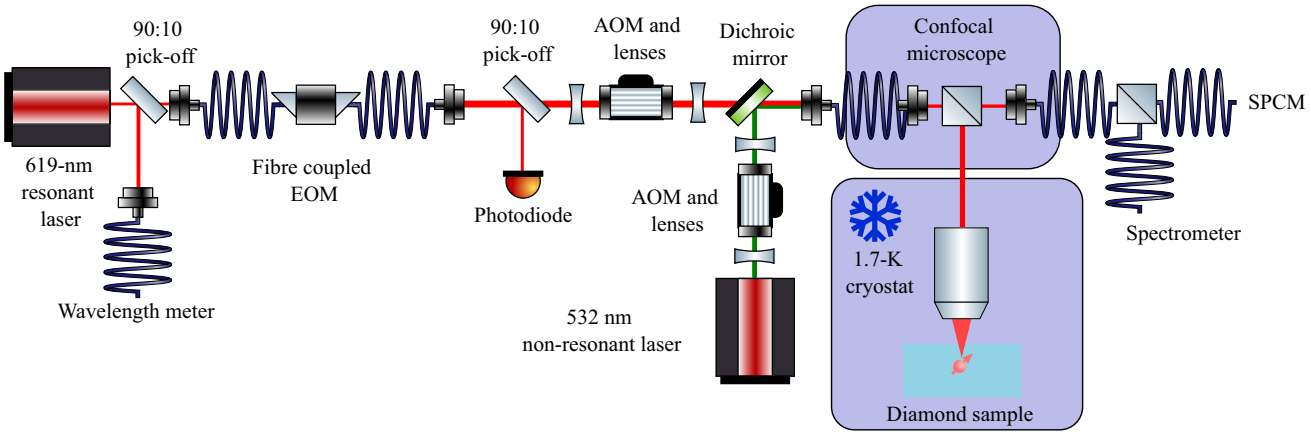

FIG. 7. A diagram of setup one, used for experiments on sample UC1. AOM, acousto-optic modulator; EOM, electro-optic modulator; SPCM, single-photon-counting module.

that the cut-on frequency was 603 nm to collect only the phonon-sideband (PSB) emission.

All resonant measurements in setup one were taken using chirped-optical-resonance excitation (CORE). A linearly chirped microwave pulse from an arbitrary wave form generator (Tektronix AWG70002A) (AWG) via a microwave amplifier (Mini-Circuits ZX60-83LN12+) and a bias tee (Mini-Circuits ZFBT-6G+) were applied to an electro-optic modulator (EOM; Jenoptik AM635) to produce laser sidebands, the frequency of which was swept over several gigahertz within a few microseconds. The EOM was kept locked to its interferometric minimum using a lock-in amplifier and a proportional-integral-differential (PID) loop (Red Pitaya, STEMlab 125-10). The collected PSB was sent to a single-photon-counting module (SPCM-AQRH-TR), which generated TTL pulses sent to a time-to-digital converter (Swabian Timetagger20). The start of a frequency sweep was triggered from the internal trigger of the AWG and also sent to the Timetagger20 to synchronize the measurement, creating a histogram where the time axis also represented the frequency sweep, matching the rf chirp. In this way, the resonance of an emitter could be swept over rapidly, avoiding any pumping effects and collecting statistics that could be used to remove drifts and emitter instability from the measurement.

2. Setup two

The WFPLE experiments were performed in a Montana systems cryostat at 5 K, using sample UC2. A similar confocal setup was used, with the addition of a lens focused on the back plane of the $4f$ system to give wide-field illumination and a Photometrics Cascade 1K electron-multiplying charge-coupled device (EMCCD) camera to image the entire objective field of view (see Fig. 8). WFPLE scans were performed at each selected implant region by scanning the M^2 system output frequency across an approximately 16-GHz range in 4-MHz steps, taking an image at each step. The locations and frequencies of all emitters in a field of view were labeled for each region and the PLE spectrum was generated from the WFPLE data by performing a Gaussian spatial average of the pixels surrounding the emitter location. Fits were performed as described in the main text on these PLE data to extract the emitter parameters.

3. Setup three

Sample UC3 was a nanofabricated diamond sample implanted with isotopically selected ^{117}Sn [40]. The resonant measurements used the CORE technique through confocal collection and excitation but the device was instead housed in a Bluefors LD250 He dilution refrigerator at 3.5 K.

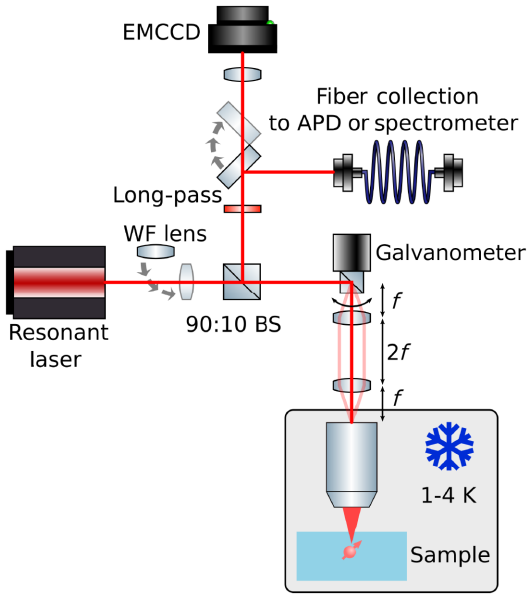

FIG. 8. A diagram of the optical setup used for the wide-field photoluminescence excitation experiments on sample UC2. APD, avalanche photodiode; BS, beam splitter.

APPENDIX C: DENSITY-FUNCTIONAL THEORY CALCULATIONS

As discussed in the main text, the hyperfine interaction is parametrized by two matrices corresponding to the Fermi-contact interaction ($\mathbf{A}_{\mathrm{FC}}$) and the dipole-dipole interaction ($\mathbf{A}_{\mathrm{DD}}$). The Fermi-contact term, A_{FC}, depends only on the spin density at the nucleus and so must be completely isotropic. It can therefore be expressed as the identity matrix times the parameter A_{FC}:

$$A_{\mathrm{FC}} = \frac{2\pi}{3} g_I \mu_N g_e \mu_B \hbar^2 \rho_S(0), \tag{C1}$$

where $\rho_S = \rho_\uparrow - \rho_\downarrow$ is the spin density, the difference between the density of spin-up and spin-down electrons $\rho_{\uparrow/\downarrow}$ around the defect. The term A_{DD} depends on the spin-density distribution around the nucleus and is therefore not isotropic in general. It can be expressed as

$$\mathbf{A}_{\mathrm{DD}} = \frac{\mu_0}{4\pi} g_I \mu_N g_e \mu_B \hbar^2 \int d\mathbf{r} \left(\frac{\mathbf{rr}}{r^5} - \frac{\mathbf{I}}{r^3} \right) \rho_S(\mathbf{r}), \tag{C2}$$

where $\mathbf{r}$ is the distance from the nucleus.

We used the QE-GIPAW package [71] within the QUANTUM ESPRESSO plane-wave DFT code [45]. Precise evaluation of Fermi contact and dipole-dipole interaction requires very accurate evaluation of the spin density in the vicinity of the nucleus. The QE-GIPAW package uses the gauge-including projector augmented wave (GIPAW) [72] method to reconstruct the valence electron orbitals near the nucleus, as well as core relaxation [73] to find the spin density at the nucleus. We performed these calculations using

the Perdew-Burke-Ernzerhof (PBE) functional [74] with the defect in its D_{3d}-symmetric configuration embedded in a $4 \times 4 \times 4$ cubic (512-atom) supercell.

We also performed excited-state calculations to find the spin density and hyperfine properties for the E_u state. These were performed with the same functional and supercell as the E_g calculation; however, we used the ΔSCF method to constrain the hole to one of the e_u Kohn-Sham orbitals [36,75]. To converge to the proper E_u state with the occupation constraint, we used a modified version of QUANTUM ESPRESSO, which implements the maximum-overlap method [76] during the self-consistent field loop to update the occupations.

The PBE functional is generally accepted to not be as accurate as more sophisticated hybrid functionals such as HSE06, which are typically used in state-of-the-art DFT calculations of defect centers in diamond [36,75,77,78]. PBE is known, in particular, to underestimate excited-state energies compared to hybrid functionals. However, as we are not concerned with the excited-state energy and only with the distribution of spin near the nuclei in the ground and excited states, we find that the computationally cheaper PBE functional is sufficient, as evidenced by the reasonable agreement between the theory and experiment. While switching to a hybrid functional may improve the accuracy, other effects such as finite supercell size, exclusion of the Jahn-Teller effect, and numerical errors in the projection of the projector-augmented-wave orbitals are likely larger contributors to the error in the hyperfine-interaction calculations.

APPENDIX D: ADDITIONAL ELECTRONUCLEAR HAMILTONIAN TERMS

The total hyperfine Hamiltonian is written as

$$\hat{H}_{\mathrm{HF}} = \hat{H}_{\mathrm{FC}} + \hat{H}_{\mathrm{DD}} + \hat{H}_{\mathrm{IOC}} + \hat{H}_{Q}, \tag{D1}$$

where $\hat{H}_{\mathrm{FC}}$ is the Fermi-contact term and $\hat{H}_{\mathrm{DD}}$ is the dipole-dipole term discussed in the main text. We briefly discuss the additional terms $\hat{H}_{\mathrm{IOC}}$ and $\hat{H}_{Q}$ shown in Eq. (D1).

The nuclear spin-orbit coupling (IOC) term, $\hat{H}_{\mathrm{IOC}}$, arises from the interaction of the nuclear spin with the magnetic field caused by the orbital motion of the hole around the defect center. It can be expressed as

$$\hat{H}_{\mathrm{IOC}} = -\frac{\mu_0}{4\pi}\frac{2g_I\mu_B\mu_N}{\hbar^2}\frac{\hat{\mathbf{L}}\cdot\hat{\mathbf{I}}}{r^3}. \tag{D2}$$

By analogy with the electronic spin-orbit coupling term, which is of the form $\hat{H}_{\mathrm{SOC}} = \lambda\hat{\mathbf{L}}\cdot\hat{\mathbf{S}}$ [34,79], we can infer that in the basis defined in Eq. (1), this reduces to

$$\hat{H}_{\mathrm{IOC}} = \frac{1}{2}\upsilon\sigma_z^{\mathrm{orb}}\hat{I}_z, \tag{D3}$$

where υ is a parameter quantifying the nuclear spin-orbit interaction. This term results in an energy shift depending on the degree of alignment of the nuclear and orbital degrees of freedom. At zero strain, this would change the spacing between the hyperfine levels to $1/2(A_{\mathrm{FC}} + A_{\mathrm{DD}} \pm \upsilon)$, with the sign depending on whether the hole is in the upper or lower branch. First-principles calculations can be employed to find the numerical value of this parameter; however, we expect it to be negligibly small for two reasons. First, the r^{-3} component of Eq. (D2) greatly suppresses the IOC interaction to be at most roughly as strong as the dipole-dipole interaction (<5% of the total hyperfine interaction). Second, the orbital magnetic term in Eq. (6), $\hat{H}_L = q\mu_B\hat{\mathbf{L}}\cdot\mathbf{B}$, is known to have a small effective response $q \approx 0.1$. This can be attributed to a decreased effective orbital angular momentum due to the presence of the lattice. We would expect this effect to further decrease the IOC, making this term roughly 3 orders of magnitude smaller than the total hyperfine interaction discussed in the paper. We leave it to future theoretical and experimental work to identify the value of this nuclear spin-orbit parameter υ.

The quadrupole interaction term $\hat{H}_Q$ arises from the nonspherical charge distribution of nuclear spins with $I > 1/2$ and is zero for $I \leq 1/2$. It is therefore only applicable to the spin-9/2 isotope ^{73}Ge discussed in this paper. The quadrupole interaction term results in a energy shift dependent on the gradient of the electric field at the location of the nucleus and takes the form

$$\hat{H}_Q = \hat{\mathbf{I}}\cdot\mathbf{Q}\cdot\hat{\mathbf{I}}, \tag{D4}$$

where $\mathbf{Q}$ is a matrix proportional to the electric field curvature at the nucleus and the nuclear quadrupole moment. If no external field is applied, the electric field curvature can only come from the electronic distribution around the defect. Similar to the hyperfine dipole-dipole interaction matrix $\mathbf{A}_{\mathrm{DD}}$, the D_{3d} symmetry of the defect restricts the matrix $\mathbf{Q}$ to be diagonal in the basis defined in Eq. (1), with $-2Q_{xx} = -2Q_{yy} = Q_{zz} = Q$. In the large electronic spin-orbit coupling limit discussed in Sec. II, the quadrupole coupling creates an anharmonic shift of Qm_J^2 of the eigenstates $|\uparrow/\downarrow\rangle|m_J\rangle$. If the nuclear spin sublevels are to be addressed individually, the anharmonicity sets the speed at which they can be manipulated, as a Rabi frequency exceeding the anharmonicity will cause unwanted driving of the wrong transition. From DFT, we estimate the parameter $Q = 4.3$ MHz for ^{73}GeV$^-$ in the ground state and therefore only causes a shift of the energy levels which is much smaller than the large A_{FC} Fermi contact. We are therefore justified in neglecting it in the main discussion in the paper.

Finally, we briefly discuss the effect of the Jahn-Teller distortion on the defect. The Jahn-Teller effect is a symmetry-breaking distortion that occurs due to unequal

TABLE III. A comparison of the hyperfine coupling for $^{29}SiV^-$ in the D_{3d} and C_{2h} configurations.

Configuration	A_{FC} (MHz)	A_{DD}^{xx} (MHz)	A_{DD}^{yy} (MHz)	A_{DD}^{zz} (MHz)
D_{3d}	54.4	1.17	1.17	−2.34
C_{2h}	49.6	−0.456	−0.456	3.16

occupation in degenerate orbitals. In the case of the group-IV color-center defects, the Jahn-Teller effect causes a distortion from D_{3d} to one of three equivalent C_{2h}-symmetric configurations. This distortion affects the distribution of the spin density, ρ_S, around the dopant nucleus. The hyperfine-interaction parameters A_{FC} in Eq. (C1) and A_{DD} in Eq. (C2) are therefore affected by this distortion, resulting in a shift of the isotropic term,

$$A_{FC}^{C_{2h}} = A_{FC}^{D_{3d}} + \delta A_{FC}, \tag{D5}$$

and a shift of the anisotropic terms,

$$A_{xx/yy}^{C_{2h}} = -\frac{1}{2}\left(A_{DD}^{D_{3d}} + \delta A_{DD}\right) \pm \delta A_{\perp}$$
$$A_{zz}^{C_{2h}} = A_{DD}^{D_{3d}} + \delta A_{DD}. \tag{D6}$$

We estimate the size of these parameters by comparing the hyperfine parameters for SiV^- in the D_{3d} and C_{2h} configurations in a $3 \times 3 \times 3$ cubic (216-atom) supercell, with the results shown in Table III. For the 216-atom supercell, the results imply $\delta A_{FC} = -4.8$ MHz, $\delta A_{DD} = 5.5$ MHz, and $\delta A_{\perp} < 0.01$ MHz. The distortion manifests mostly as a shift in the D_{3d} values, with the symmetry-breaking component $\delta A_{\perp}$ remaining very small, giving some insight into why the C_{H0} line does not split at zero strain due to Jahn-Teller. Given these results, we estimate that Jahn-Teller distortion changes the magnitude of the hyperfine coupling by approximately 10% of the total value. This potentially explains a portion of the error in the DFT calculations in the main text, where Jahn-Teller is neglected. A complete treatment of the Jahn-Teller effect would require

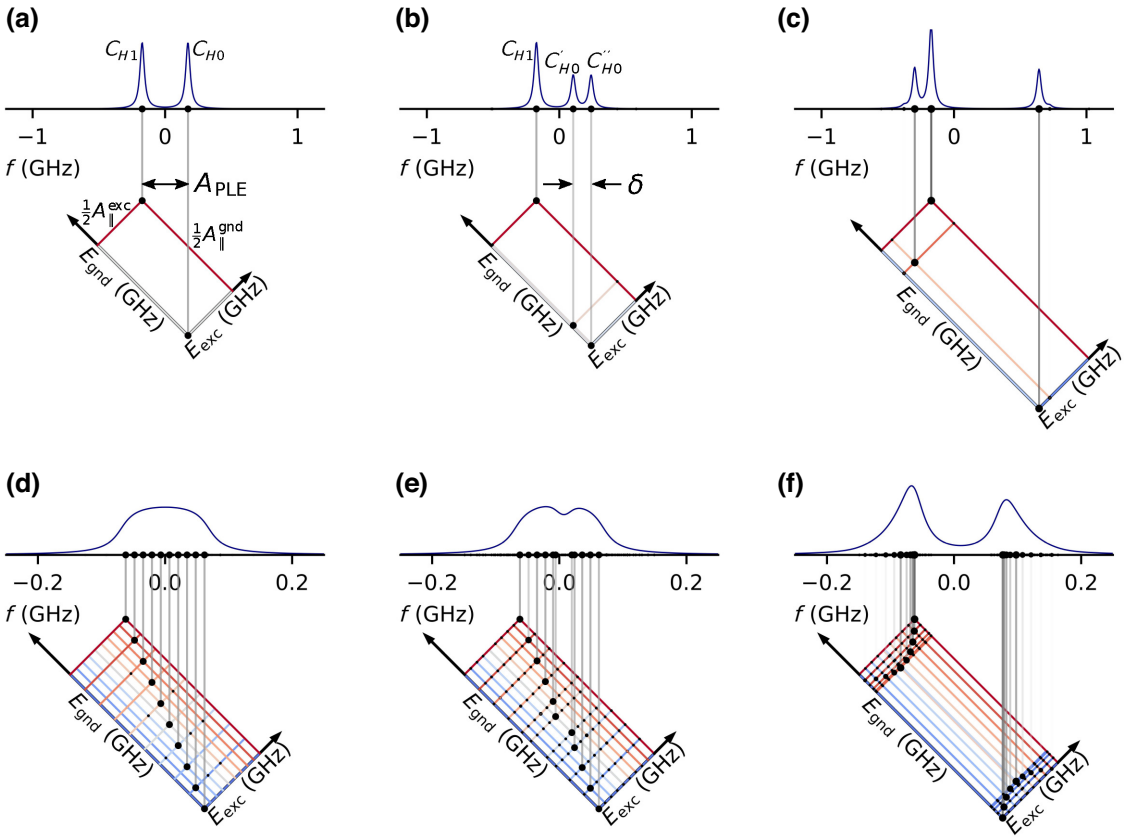

FIG. 9. A visualization of the spectra for (a)–(c) $^{117}SnV^-$ and (d)–(f) $^{73}GeV^-$, using predicted hyperfine parameters at various strains, α: (a) $\alpha = 0.0$ GHz; (b) $\alpha = 42.5$ GHz; (c) $\alpha = 425.0$ GHz; (d) $\alpha = 0.0$ GHz; (e) $\alpha = 9.05$ GHz; (f) $\alpha = 90.5$ GHz. The bottom half of each plot shows the hyperfine levels in the ground or excited state. At each intersection, a line the intensity of which is proportional to the strength of the corresponding transition is plotted. Each transition line aligns with the relative frequency of the optical transition and the resulting predicted spectrum is shown in the upper half of the plot.

inclusion of the Jahn-Teller phonon modes to find the combined spin-phonon vibronic states [36], where the effective hyperfine interaction would then be averaged over the vibronic configurations. Since Jahn-Teller does not qualitatively change the predictions, we leave a detailed study for future work.

APPENDIX E: VISUALIZATION OF HYPERFINE SPECTRA

In Fig. 9, we show a plot highlighting the origin of the hyperfine optical spectrum. In the lower half of each subplot, we plot the ground-state and excited-state hyperfine energy levels as a set of lines, with the color corresponding to the total angular momentum $\langle J^2 \rangle$ of that state (red being nuclear and electron spins aligned; blue antialigned). The intersection of each of the ground or excited state lines corresponds to a potential transition that can occur and a line is plotted for each transition to the upper axis, with the intensity of the line corresponding to the predicted intensity of that transition. The lower half plot is rotated and scaled in such a way that the position along the x axis of the upper half plot lines up with the transition frequency. A predicted spectrum is shown, calculated as the intensity-weighted sum of all the transitions.

It is evident that the transitions with the largest contribution are the ones between states with identical $\langle J^2 \rangle$, i.e., spin-conserving transitions. As the strain increases, the ground-state hyperfine levels start to split, as discussed in Sec. II. This effect is suppressed in the excited state due to the higher spin-orbit coupling in the E_u state.

For $^{117}SnV^-$ in Figs. 9(a)–9(c), the spectrum at zero strain consists of two peaks corresponding to transitions between the ground and excited $m_J = \pm 1$ and $m_J = 0$ levels, respectively. At higher strain, the $m_J = 0$ peaks split apart primarily due to the ground-level strain splitting, which can be seen in the spectrum in Fig. 5(c). The spectra in Fig. 5(b) are averaged over many sites, with the frequency shifted such that the lowest-energy peak is at 0. The higher-frequency peak is then reduced in intensity due to the combined effects of (1) residual spin-0 isotopes that do not have the secondary peak at all and (2) variability in the hyperfine optical splitting parameters A_{PLE} and δ from measurement noise and differences in strain between emitters.

For $^{73}GeV^-$ in Figs. 9(d)–9(f), the strain causes the flat-topped peak to split into two peaks corresponding to the transitions between the $J = 5$ levels at lower energy and the $J = 4$ levels at higher energy. We note that the predicted spectrum is shown for a near-lifetime-limited line width and that these features are not easily visible in the WFPLE GeV^- spectra shown in the main text.

We also highlight the effect of a magnetic field aligned along the z direction on $^{73}GeV^-$ in Fig. 10. As the B field increases, the states containing terms with electronic

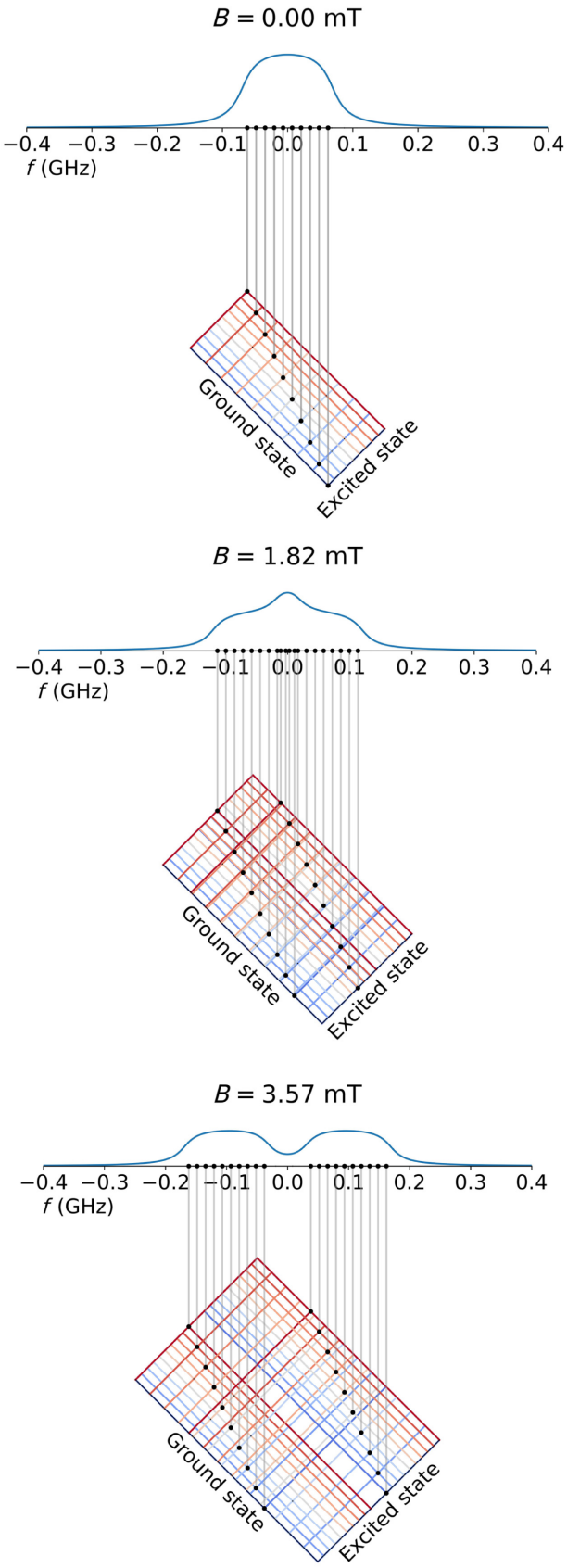

FIG. 10. A visualization of the spectra for $^{73}GeV^-$ as a function of the B field.

states $|\uparrow\rangle$ and $|\downarrow\rangle$ are shifted in opposite directions. The ground and excited states are shifted by differing amounts due to the difference in orbital magnetic field response in the ground state (excited state), $q_{\mathrm{gnd(exc)}}$. Note that q_{exc} has been artificially decreased to keep the figure compact. The same general phenomenon occurs with the true experimental value, albeit at the higher fields observed in Fig. 4(d).

As the magnetic field increases, the two groups of transitions stop overlapping completely as they do at zero field. For sufficiently strong fields, the two groups of transitions become fully separated and two flat-topped peaks become apparent in the spectrum. At intermediate field strengths, the transitions near zero detuning still overlap, causing a characteristic bump at the center of the transition peak, with two broad shoulders.

[1] L. Childress, D. J. Twitchen, B. Hensen, M. S. Blok, L. Robledo, R. Hanson, G. Koolstra, H. Bernien, M. Markham, T. H. Taminiau, and W. Pfaff, Heralded entanglement between solid-state qubits separated by three metres, Nature **497**, 86 (2013).

[2] N. Kalb, A. A. Reiserer, P. C. Humphreys, J. J. Bakermans, S. J. Kamerling, N. H. Nickerson, S. C. Benjamin, D. J. Twitchen, M. Markham, and R. Hanson, Entanglement distillation between solid-state quantum network nodes, Science **356**, 928 (2017).

[3] M. Pompili, S. L. Hermans, S. Baier, H. K. Beukers, P. C. Humphreys, R. N. Schouten, R. F. Vermeulen, M. J. Tiggelman, L. dos Santos Martins, B. Dirkse, S. Wehner, and R. Hanson, Realization of a multinode quantum network of remote solid-state qubits, Science **372**, 259 (2021).

[4] P.-J. Stas, Y. Q. Huan, B. Machielse, E. N. Knall, A. Suleymanzade, B. Pingault, M. Sutula, S. W. Ding, C. M. Knaut, D. R. Assumpcao, Y.-C. Wei, M. K. Bhaskar, R. Riedinger, D. D. Sukachev, H. Park, M. Lončar, D. S. Levonian, and M. D. Lukin, Robust multi-qubit quantum network node with integrated error detection, Science **378**, 557 (2022).

[5] T. Neuman, M. Eichenfield, M. E. Trusheim, L. Hackett, P. Narang, and D. Englund, A phononic interface between a superconducting quantum processor and quantum networked spin memories, npj Quantum Inf. **7**, 1 (2021).

[6] H. Raniwala, S. Krastanov, L. Hackett, M. Eichenfield, D. R. Englund, and M. E. Trusheim, Spin-phonon-photon strong coupling in a piezomechanical nanocavity, preprint arXiv:2202.11291 (2022).

[7] T. Staudacher, F. Shi, S. Pezzagna, J. Meijer, J. Du, C. A. Meriles, F. Reinhard, and J. Wrachtrup, Nuclear magnetic resonance spectroscopy on a (5-nanometer)^3 sample volume, Science **339**, 561 (2013).

[8] D. Kim, M. I. Ibrahim, C. Foy, M. E. Trusheim, R. Han, and D. R. Englund, A CMOS-integrated quantum sensor based on nitrogen-vacancy centres, Nat. Electron. **2**, 284 (2019).

[9] E. R. Eisenach, J. F. Barry, M. F. O'Keeffe, J. M. Schloss, M. H. Steinecker, D. R. Englund, and D. A. Braje, Cavity-enhanced microwave readout of a solid-state spin sensor, Nat. Commun. **12**, 1 (2021).

[10] D. Hucul, I. V. Inlek, G. Vittorini, C. Crocker, S. Debnath, S. M. Clark, and C. Monroe, Modular entanglement of atomic qubits using photons and phonons, Nat. Phys. **11**, 37 (2015).

[11] H. Choi, M. Pant, S. Guha, and D. Englund, Percolation-based architecture for cluster state creation using photon-mediated entanglement between atomic memories, npj Quantum Inf. **5**, 1 (2019).

[12] M. Atatüre, D. Englund, N. Vamivakas, S. Y. Lee, and J. Wrachtrup, Material platforms for spin-based photonic quantum technologies, Nat. Rev. Mater. **3**, 38 (2018).

[13] C. T. Nguyen, D. D. Sukachev, M. K. Bhaskar, B. Machielse, D. S. Levonian, E. N. Knall, P. Stroganov, C. Chia, M. J. Burek, R. Riedinger, H. Park, M. Lončar, and M. D. Lukin, An integrated nanophotonic quantum register based on silicon-vacancy spins in diamond, Phys. Rev. B **100**, 165428 (2019).

[14] B. Machielse, S. Bogdanovic, S. Meesala, S. Gauthier, M. J. Burek, G. Joe, M. Chalupnik, Y. I. Sohn, J. Holzgrafe, R. E. Evans, C. Chia, H. Atikian, M. K. Bhaskar, D. D. Sukachev, L. Shao, S. Maity, M. D. Lukin, and M. Lončar, Quantum interference of electromechanically stabilized emitters in nanophotonic devices, Phys. Rev. X **9**, 031022 (2019).

[15] N. H. Wan, T. J. Lu, K. C. Chen, M. P. Walsh, M. E. Trusheim, L. De Santis, E. A. Bersin, I. B. Harris, S. L. Mouradian, I. R. Christen, E. S. Bielejec, and D. Englund, Large-scale integration of artificial atoms in hybrid photonic circuits, Nature **583**, 226 (2020).

[16] A. E. Rugar, C. Dory, S. Aghaeimeibodi, H. Lu, S. Sun, S. D. Mishra, Z. X. Shen, N. A. Melosh, and J. Vučković, Narrow-linewidth tin-vacancy centers in a diamond waveguide, ACS Photonics **7**, 2356 (2020).

[17] J. Arjona Martínez, R. A. Parker, K. C. Chen, C. M. Purser, L. Li, C. P. Michaels, A. M. Stramma, R. Debroux, I. B. Harris, M. Hayhurst Appel, E. C. Nichols, M. E. Trusheim, D. A. Gangloff, D. Englund, and M. Atatüre, Photonic indistinguishability of the tin-vacancy center in nanostructured diamond, Phys. Rev. Lett. **129**, 173603 (2022).

[18] L. De Santis, M. E. Trusheim, K. C. Chen, and D. R. Englund, Investigation of the Stark effect on a centrosymmetric quantum emitter in diamond, Phys. Rev. Lett. **127**, 147402 (2021).

[19] B. Pingault, D. D. Jarausch, C. Hepp, L. Klintberg, J. N. Becker, M. Markham, C. Becher, and M. Atatüre, Coherent control of the silicon-vacancy spin in diamond, Nat. Commun. **8**, 1 (2017).

[20] R. Debroux, C. P. Michaels, C. M. Purser, N. Wan, M. E. Trusheim, J. Arjona Martínez, R. A. Parker, A. M. Stramma, K. C. Chen, L. De Santis, E. M. Alexeev, A. C. Ferrari, D. Englund, D. A. Gangloff, and M. Atatüre, Quantum control of the tin-vacancy spin qubit in diamond, Phys. Rev. X **11**, 041041 (2021).

[21] J. N. Becker, B. Pingault, D. Groß, M. Gündoğan, N. Kukharchyk, M. Markham, A. Edmonds, M. Atatüre, P. Bushev, and C. Becher, All-optical control of the silicon-vacancy spin in diamond at millikelvin temperatures, Phys. Rev. Lett. **120**, 183602 (2018).

[22] C. T. Nguyen, D. D. Sukachev, M. K. Bhaskar, B. Machielse, D. S. Levonian, E. N. Knall, P. Stroganov, R. Riedinger, H. Park, M. Lončar, and M. D. Lukin, Quantum

network nodes based on diamond qubits with an efficient nanophotonic interface, Phys. Rev. Lett. **123**, 183602 (2019).

[23] C. P. Michaels, J. A. Martinez, R. Debroux, R. A. Parker, A. M. Stramma, L. I. Huber, C. M. Purser, M. Atature, and D. A. Gangloff, Multidimensional cluster states using a single spin-photon interface coupled strongly to an intrinsic nuclear register, Quantum **5**, 565 (2021).

[24] A. Russo, E. Barnes, and S. E. Economou, Generation of arbitrary all-photonic graph states from quantum emitters, New J. Phys. **21**, 055002 (2019).

[25] A. Russo, E. Barnes, and S. E. Economou, Photonic graph state generation from quantum dots and color centers for quantum communications, Phys. Rev. B **98**, 085303 (2018).

[26] S. Felton, A. M. Edmonds, M. E. Newton, P. M. Martineau, D. Fisher, D. J. Twitchen, and J. M. Baker, Hyperfine interaction in the ground state of the negatively charged nitrogen vacancy center in diamond, Phys. Rev. B—Condens. Matter Mater. Phys. **79**, 075203 (2009).

[27] K. Szász, T. Hornos, M. Marsman, and A. Gali, Hyperfine coupling of point defects in semiconductors by hybrid density functional calculations: The role of core spin polarization, Phys. Rev. B—Condens. Matter Mater. Phys. **88**, 75202 (2013).

[28] R. Kuate Defo, E. Kaxiras, and S. L. Richardson, Calculating the hyperfine tensors for group-IV impurity-vacancy centers in diamond using hybrid density functional theory, Phys. Rev. B **104**, 75158 (2021).

[29] M. H. Abobeih, Y. Wang, J. Randall, S. J. Loenen, C. E. Bradley, M. Markham, D. J. Twitchen, B. M. Terhal, and T. H. Taminiau, Fault-tolerant operation of a logical qubit in a diamond quantum processor, Nature **606**, 884 (2022).

[30] C. E. Bradley, S. W. de Bone, P. F. Möller, S. Baier, M. J. Degen, S. J. Loenen, H. P. Bartling, M. Markham, D. J. Twitchen, R. Hanson, D. Elkouss, and T. H. Taminiau, Robust quantum-network memory based on spin qubits in isotopically engineered diamond, npj Quantum Inf. **8**, 1 (2022).

[31] C. E. Bradley, J. Randall, M. H. Abobeih, R. C. Berrevoets, M. J. Degen, M. A. Bakker, M. Markham, D. J. Twitchen, and T. H. Taminiau, A ten-qubit solid-state spin register with quantum memory up to one minute, Phys. Rev. X **9**, 031045 (2019).

[32] W. Pfaff, T. H. Taminiau, L. Robledo, H. Bernien, M. Markham, D. J. Twitchen, and R. Hanson, Demonstration of entanglement-by-measurement of solid-state qubits, Nat. Phys. **9**, 29 (2013).

[33] E. Neu, C. Hepp, M. Hauschild, S. Gsell, M. Fischer, H. Sternschulte, D. Steinmüller-Nethl, M. Schreck, and C. Becher, Low-temperature investigations of single silicon vacancy colour centres in diamond, New J. Phys. **15**, 43005 (2013).

[34] C. Hepp, T. Müller, V. Waselowski, J. N. Becker, B. Pingault, H. Sternschulte, D. Steinmüller-Nethl, A. Gali, J. R. Maze, M. Atatüre, and C. Becher, Electronic Structure of the Silicon Vacancy Color Center in Diamond, Phys. Rev. Lett. **112**, 036405 (2014).

[35] K. D. Jahnke, A. Sipahigil, J. M. Binder, M. W. Doherty, M. Metsch, L. J. Rogers, N. B. Manson, M. D. Lukin, and F. Jelezko, Electron-phonon processes of the silicon-vacancy centre in diamond, New J. Phys. **17**, 043011 (2015).

[36] G. G. Thiering and A. Gali, *Ab initio* magneto-optical spectrum of group-IV vacancy color centers in diamond, Phys. Rev. X **8**, 21063 (2018).

[37] L. J. Rogers, K. D. Jahnke, M. H. Metsch, A. Sipahigil, J. M. Binder, T. Teraji, H. Sumiya, J. Isoya, M. D. Lukin, P. Hemmer, and F. Jelezko, All-optical initialization, readout, and coherent preparation of single silicon-vacancy spins in diamond, Phys. Rev. Lett. **113**, 263602 (2014).

[38] C. Adambukulam, H. Vallabhapurapu, B. Johnson, A. Morello, and A. Laucht, Abstract: F74.00011: All Optical Initialisation and Readout and Coherent Population Trapping of a Single Germanium Vacancy in Diamond, *APS March Meeting 2023, Las Vegas, Nevada* (2023).

[39] M. E. Trusheim, B. Pingault, N. H. Wan, M. Gündoğan, L. De Santis, R. Debroux, D. Gangloff, C. Purser, K. C. Chen, M. Walsh, J. J. Rose, J. N. Becker, B. Lienhard, E. Bersin, I. Paradeisanos, G. Wang, D. Lyzwa, A. R. Montblanch, G. Malladi, H. Bakhru, A. C. Ferrari, I. A. Walmsley, M. Atatüre, and D. Englund, Transform-limited photons from a coherent tin-vacancy spin in diamond, Phys. Rev. Lett. **124**, 023602 (2020).

[40] R. A. Parker, J. A. Martínez, K. C. Chen, A. M. Stramma, I. B. Harris, C. P. Michaels, M. E. Trusheim, M. H. Appel, C. M. Purser, W. G. Roth, D. Englund, and M. Atatüre, A diamond nanophotonic interface with an optically accessible deterministic electronuclear spin register, preprint arXiv:2305.18923 (2023).

[41] M. Tinkham, *Group Theory and Quantum Mechanics* (Dover Publications, Mineola, New York, 1992), p. 340.

[42] M. W. Doherty, N. B. Manson, P. Delaney, and L. C. Hollenberg, The negatively charged nitrogen-vacancy centre in diamond: The electronic solution, New J. Phys. **13**, 025019 (2011).

[43] S. Meesala, Y. I. Sohn, B. Pingault, L. Shao, H. A. Atikian, J. Holzgrafe, M. Gündoğan, C. Stavrakas, A. Sipahigil, C. Chia, R. Evans, M. J. Burek, M. Zhang, L. Wu, J. L. Pacheco, J. Abraham, E. Bielejec, M. D. Lukin, M. Atatüre, and M. Lončar, Strain engineering of the silicon-vacancy center in diamond, Phys. Rev. B **97**, 205444 (2018).

[44] M. L. Munzarová, in *Calculation of NMR and EPR Parameters* (Wiley-VCH Verlag GmbH & Co. KGaA, Weinheim, 2004), p. 461.

[45] P. Giannozzi, S. Baroni, N. Bonini, M. Calandra, R. Car, C. Cavazzoni, D. Ceresoli, G. L. Chiarotti, M. Cococcioni, I. Dabo, A. Dal Corso, S. De Gironcoli, S. Fabris, G. Fratesi, R. Gebauer, U. Gerstmann, C. Gougoussis, A. Kokalj, M. Lazzeri, L. Martin-Samos, N. Marzari, F. Mauri, R. Mazzarello, S. Paolini, A. Pasquarello *et al.*, QUANTUM ESPRESSO: A modular and open-source software project for quantum simulations of materials, J. Phys. Condens. Matter **21**, 395502 (2009).

[46] G. Feher, Observation of nuclear magnetic resonances via the electron spin resonance line, Phys. Rev. **103**, 834 (1956).

[47] G. Pica, G. Wolfowicz, M. Urdampilleta, M. L. Thewalt, H. Riemann, N. V. Abrosimov, P. Becker, H. J. Pohl, J. J. Morton, R. N. Bhatt, S. A. Lyon, and B. W. Lovett, Hyperfine Stark effect of shallow donors in silicon, Phys. Rev. B—Condens. Matter Mater. Phys. **90**, 195204 (2014).

[48] L. B. Knight and W. Weltner, Hyperfine interaction, chemical bonding, and isotope effect in ZnH, CdH, and HgH molecules, J. Chem. Phys. **55**, 2061 (1971).

[49] M. K. Bhaskar, D. D. Sukachev, A. Sipahigil, R. E. Evans, M. J. Burek, C. T. Nguyen, L. J. Rogers, P. Siyushev, M. H. Metsch, H. Park, F. Jelezko, M. Lončar, and M. D. Lukin, Quantum nonlinear optics with a germanium-vacancy color center in a nanoscale diamond waveguide, Phys. Rev. Lett. **118**, 223603 (2017).

[50] M. Sutula, I. Christen, E. Bersin, M. P. Walsh, K. C. Chen, J. Mallek, A. Melville, M. Titze, E. S. Bielejec, S. Hamilton, D. Braje, P. B. Dixon, and D. R. Englund, Large-scale optical characterization of solid-state quantum emitters, Nat. Mater. (2023).

[51] A. Dietrich, K. D. Jahnke, J. M. Binder, T. Teraji, J. Isoya, L. J. Rogers, and F. Jelezko, Isotopically varying spectral features of silicon-vacancy in diamond, New J. Phys. **16**, 113019 (2014).

[52] E. A. Ekimov, S. G. Lyapin, K. N. Boldyrev, M. V. Kondrin, R. Khmelnitskiy, V. A. Gavva, T. V. Kotereva, and M. N. Popova, Germanium-vacancy color center in isotopically enriched diamonds synthesized at high pressures, JETP Lett. **102**, 701 (2015).

[53] E. A. Ekimov, V. S. Krivobok, S. G. Lyapin, P. S. Sherin, V. A. Gavva, and M. V. Kondrin, Anharmonicity effects in impurity-vacancy centers in diamond revealed by isotopic shifts and optical measurements, Phys. Rev. B **95**, 094113 (2017).

[54] T. Iwasaki, F. Ishibashi, Y. Miyamoto, Y. Doi, S. Kobayashi, T. Miyazaki, K. Tahara, K. D. Jahnke, L. J. Rogers, B. Naydenov, F. Jelezko, S. Yamasaki, S. Nagamachi, T. Inubushi, N. Mizuochi, and M. Hatano, Germanium-vacancy single color centers in diamond, Sci. Rep. **5**, 12882 (2015).

[55] Y. Narita, P. Wang, K. Ikeda, K. Oba, Y. Miyamoto, T. Taniguchi, S. Onoda, M. Hatano, and T. Iwasaki, Multiple tin-vacancy centers in diamond with nearly identical photon frequency and linewidth, Phys. Rev. Appl. **19**, 024061 (2023).

[56] J. Görlitz, D. Herrmann, P. Fuchs, T. Iwasaki, T. Taniguchi, D. Rogalla, D. Hardeman, P. O. Colard, M. Markham, M. Hatano, and C. Becher, Coherence of a charge stabilised tin-vacancy spin in diamond, npj Quantum Inf. **8**, 1 (2022).

[57] M. Titze, H. Byeon, A. Flores, J. Henshaw, C. T. Harris, A. M. Mounce, and E. S. Bielejec, In situ ion counting for improved implanted ion error rate and silicon vacancy yield uncertainty, Nano Lett. **22**, 3212 (2022).

[58] V. Chandrasekaran, M. Titze, A. R. Flores, D. Campbell, J. Henshaw, A. C. Jones, E. S. Bielejec, and H. Htoon, High-yield deterministic focused ion beam implantation of quantum defects enabled by in situ photoluminescence feedback, Adv. Sci. **2023**, 2300190 (2023).

[59] J. J. Bollinger, J. D. Prestage, W. M. Itano, and D. J. Wineland, Laser-cooled-atomic frequency standard, Phys. Rev. Lett. **54**, 1000 (1985).

[60] J. M. Kindem, A. Ruskuc, J. G. Bartholomew, J. Rochman, Y. Q. Huan, and A. Faraon, Control and single-shot readout of an ion embedded in a nanophotonic cavity, Nature **580**, 201 (2020).

[61] M. Onizhuk, K. C. Miao, J. P. Blanton, H. Ma, C. P. Anderson, A. Bourassa, D. D. Awschalom, and G. Galli, Probing the coherence of solid-state qubits at avoided crossings, PRX Quantum **2**, 10311 (2021).

[62] J. N. Becker, B. Pingault, D. Groß, M. Gündoğan, N. Kukharchyk, M. Markham, A. Edmonds, M. Atatüre, P. Bushev, and C. Becher, All-optical control of the silicon-vacancy spin in diamond at millikelvin temperatures, Phys. Rev. Lett. **120**, 053603 (2018).

[63] S. Asaad, V. Mourik, B. Joecker, M. A. I. Johnson, A. D. Baczewski, H. R. Firgau, M. T. Mądzik, V. Schmitt, J. J. Pla, F. E. Hudson, K. M. Itoh, J. C. McCallum, A. S. Dzurak, A. Laucht, and A. Morello, Coherent electrical control of a single high-spin nucleus in silicon, Nature **579**, 205 (2019).

[64] M. Prabhu, C. Errando-Herranz, L. De Santis, I. Christen, C. Chen, C. Gerlach, and D. Englund, Individually addressable and spectrally programmable artificial atoms in silicon photonics, Nat. Commun. **14**, 1 (2023).

[65] D. B. Higginbottom, A. T. Kurkjian, C. Chartrand, M. Kazemi, N. A. Brunelle, E. R. MacQuarrie, J. R. Klein, N. R. Lee-Hone, J. Stacho, M. Ruether, C. Bowness, L. Bergeron, A. DeAbreu, S. R. Harrigan, J. Kanaganayagam, D. W. Marsden, T. S. Richards, L. A. Stott, S. Roorda, K. J. Morse, M. L. Thewalt, and S. Simmons, Optical observation of single spins in silicon, Nature **607**, 266 (2022).

[66] K. C. Miao, A. Bourassa, C. P. Anderson, S. J. Whiteley, A. L. Crook, S. L. Bayliss, G. Wolfowicz, G. Thiering, P. Udvarhelyi, V. Ivády, H. Abe, T. Ohshima, Á. Gali, and D. D. Awschalom, Electrically driven optical interferometry with spins in silicon carbide, Sci. Adv. **5**, eaay0527 (2019).

[67] G. Wolfowicz, C. P. Anderson, B. Diler, O. G. Poluektov, F. J. Heremans, and D. D. Awschalom, Vanadium spin qubits as telecom quantum emitters in silicon carbide, Sci. Adv. **6**, eaaz1192 (2020).

[68] A. L. Crook, C. P. Anderson, K. C. Miao, A. Bourassa, H. Lee, S. L. Bayliss, D. O. Bracher, X. Zhang, H. Abe, T. Ohshima, E. L. Hu, and D. D. Awschalom, Purcell enhancement of a single silicon carbide color center with coherent spin control, Nano Lett. **20**, 3427 (2020).

[69] X. Wang, C. Zimmermann, M. Titze, V. Niaouris, E. R. Hansen, S. H. D'ambrosia, L. Vines, E. S. Bielejec, and K.-M. C. Fu, Properties of donor qubits in ZnO formed by indium-ion implantation, Phys. Rev. Appl. **19**, 54090 (2023).

[70] J. Görlitz, D. Herrmann, G. Thiering, P. Fuchs, M. Gandil, T. Iwasaki, T. Taniguchi, M. Kieschnick, J. Meijer, M. Hatano, A. Gali, and C. Becher, Spectroscopic investigations of negatively charged tin-vacancy centres in diamond, New J. Phys. **22**, 013048 (2020).

[71] P. Giannozzi, O. Andreussi, T. Brumme, O. Bunau, M. Buongiorno Nardelli, M. Calandra, R. Car, C. Cavazzoni, D. Ceresoli, M. Cococcioni, N. Colonna, I. Carnimeo, A. Dal Corso, S. De Gironcoli, P. Delugas, R. A. Distasio, A. Ferretti, A. Floris, G. Fratesi, G. Fugallo, R. Gebauer, U. Gerstmann, F. Giustino, T. Gorni, J. Jia *et al.*, Advanced capabilities for materials modelling with QUANTUM ESPRESSO, J. Phys. Condens. Matter **29**, 465901 (2017).

[72] C. J. Pickard and F. Mauri, All-electron magnetic response with pseudopotentials: NMR chemical shifts, Phys. Rev. B **63**, 245101 (2001).

[73] M. S. Bahramy, M. H. Sluiter, and Y. Kawazoe, Pseudopotential hyperfine calculations through perturbative core-level polarization, Phys. Rev. B—Condens. Matter Mater. Phys. **76**, 035124 (2007).

[74] J. P. Perdew, K. Burke, and M. Ernzerhof, Generalized gradient approximation made simple, Phys. Rev. Lett. **77**, 3865 (1996).

[75] C. J. Ciccarino, J. Flick, I. B. Harris, M. E. Trusheim, D. R. Englund, and P. Narang, Strong spin-orbit quenching via the product Jahn-Teller effect in neutral group IV qubits in diamond, npj Quantum Mater. **5**, 1 (2020).

[76] A. T. Gilbert, N. A. Besley, and P. M. Gill, Self-consistent field calculations of excited states using the maximum overlap method (MOM), J. Phys. Chem. A **112**, 13164 (2008).

[77] G. Thiering and A. Gali, The $(e_g \otimes e_u) \otimes E_g$ product Jahn-Teller effect in the neutral group-IV vacancy quantum bits in diamond, npj Comput. Mater. **5**, 18 (2019).

[78] I. Harris, C. J. Ciccarino, J. Flick, D. R. Englund, and P. Narang, Group-III quantum defects in diamond are stable spin-1 color centers, Phys. Rev. B **102**, 195206 (2020).

[79] C. Hepp, Ph.D. thesis, Universität des Saarlandes, 2014.